OPTICAL NONLINEARITIES AND ORDERING IN AQUEOUS AND ORGANIC COLLOIDAL PLASMONIC MATERIALS

A Thesis submitted to the faculty of
San Francisco State University
In partial fulfillment of
the requirements for
the Degree

Master of Science

In

Physics

by

Pepito Bustos Alvaro Jr.

San Francisco, California

May 2018

CERTIFICATION OF APPROVAL

I certify that I have read *Optical Nonlinearities and Ordering in Aqueous and Organic Colloidal Plasmonic Materials* by Pepito Bustos Alvaro Jr, and that in my opinion this work meets the criteria for approving a thesis submitted in partial fulfillment of the requirement for the degree Master of Science in Physics at San Francisco State University.

Zhigang Chen, Ph.D.
Professor of Physics

Huizhong Xu, Ph.D.
Associate Professor of Physics

AKM Newaz, Ph.D.
Assistant Professor of Physics

OPTICAL NONLINEARITIES AND ORDERING IN AQUEOUS AND ORGANIC COLLOIDAL PLASMONIC MATERIALS

Pepito Bustos Alvaro Jr.
San Francisco, California
2018

This thesis discusses four experiments on the ordering of gold nanorods. In the first experiment, a linearly polarized focused pump beam transmits through a solution of gold nanorods in water to create a soliton waveguide. A probe beam, linearly polarized at some angle with respect to the polarization of the pump beam, is then guided into the soliton channel. We then measure the output transmission as a function of the probe polarization to show the ordering of the nanorods in the soliton channel. Unfortunately, the results were not very reproducible. We discuss the possible reasons for experimental inconsistency and reproducibility.

In the second experiment we use a set of parallel plates powered by a variable high voltage supply to create a controlled uniform electric field. These parallel plates are between a solution of nanorods (aqueous or organic). We then shine white light and measure transmission and obtain the absorption spectrum of our ordered sample. We found the spectrum does not change with the voltage applied for our aqueous solution. But strong dependence of the spectrum on the voltage applied is observed for our organic (toluene) solution.

In the third experiment, we use a similar setup as the first, but with a toluene solution of gold nanorods. Based on results from our second experiment we found noticeable ordering of nanorods in an organic solution compared to an aqueous nanorod solution. This motived us to explore the same experiment, but with organic solvent.

In the fourth experiment, we use a pump beam to create soliton in our toluene solution of gold nanorods. We then add voltage to our parallel plates to see how an external electric field affects the non-linear action in our soliton. We also explored what happens when the pump beam power is too high and thermal effects break up the soliton. An external electric field is then added to investigate its effect on soliton formation.

These experimental studies provide a step forward for optical manipulation of nanorods and for synthesizing plasmonic nanosuspensions with tunable optical nonlinearity.

I certify that the Abstract is a correct representation of the content of this thesis.

Chair, Thesis Committee

5/21/2018
Date

PREFACE AND/OR ACKNOWLEDGEMENTS

I would like to thank my advisor and committee members, Dr. Zhigang Chen, Dr. Huizhong Xu, and Dr. Akm Newaz. I spent only about a year and a half in the optics lab, but with the guidance of Dr. Chen and Dr. Xu, I was able to get as far as I did. I want to thank our post-docs, Dr. Yinxiao and Dr. Yi Liang, for constantly brainstorming with me on my projects. I want to thank Trevor Kelly for introducing me to the optics lab and for his constant positive attitude and tenacity. Knowing his journey to get his master's degree was truly inspiring. I want to thank Stephen Nenni for his willingness to converse with me and explain things on the board. I want to thank Priti Patil for her positive attitude and constant hard work. Seeing someone work as hard as she does makes me want to do the same. I want to thank Dylan Pounds and Lisa Kotowski for being there as we got through Jackson. I want to thank Dr. Susan Lea for her unwavering discipline and her motto: "Practice doesn't make perfect. *Perfect* practice makes perfect." I want to thank Dr. Barbara Neuhauser for her willingness to help me with a letter of recommendation for the Air Force and her countless Netflix and book recommendations. I want to thank Dr. Kristan Jensen for showing me how one can simultaneously be cheerful, humble, and vastly intelligent. His office hours and general attitude made Statistical Mechanics infinitely fun. I want to thank Dr. Joseph Barranco for his enthusiastic teaching style. He was one of my professors my first semester in the graduate school and I am truly thankful for that. I want to thank Dr. Roger Bland for teaching me introductory theoretical physics and Dr. Anna Bezryadina for teaching me introductory thermal physics. Both of them helped me during a rough semester. I want to thank three amazing female physicists from my old job at Varian Medical Systems, Dr. Hsinlu Hsu, Dr. Vidhya Krishnamurthi, and Dr. Magdalena Constantin. They were extremely supportive during the time I was both working full time at Varian Medical Systems and going to San Francisco State University as a graduate student. They guided me while I was a Physics Intern and were kind faces when I became a Hardware Development Engineer. And they were supportive when I decided to quit my job to finish graduate school fulltime and then become a commission officer in the Air Force. I want to thank Jeff Everett for being an amazing project manager. He showed me what hard work and a soft-spoken attitude can accomplish. I want to thank countless more people, friends, acquaintances, work mates, lab mates, classmates for all their support and kind conversations. But lastly, I want to thank my parents. My dad, Pepito Alvaro Sr. for emphasizing the value of education. He told me that knowledge is something no one can steal from you. My mom, Adelaida Alvaro, for working harder than any human being I know. She constantly shows me what love and hard work are capable of.

TABLE OF CONTENTS

Table of Contents

LIST OF TABLES

Table Page

LIST OF FIGURES

Figures Page

LIST OF APPENDICES

Chapter 1: Introduction

1.1 Background of Solitons

In general, a soliton is a self-reinforcing solitary wave packet that maintains its shape while it propagates at a constant velocity. The first soliton was described by John Scott Russell in 1834. Russell describes his observations in a canal as a wave of translation [1, 25]:

> *I was observing the motion of a boat which was rapidly drawn along a narrow channel by a pair of horses, when the boat suddenly stopped-- not so the mass of the water in the channel which it had put in motion; it accumulated round the prow of the vessel in a state of violent agitation, then suddenly leaving it behind, rolled forward with great velocity, assuming the form of a large solitary elevation, a rounded, smooth and well-defined heap of water, which continued its course along the channel apparently without change of form or diminution of speed. I followed it on horseback, and overtook it still rolling at a rate of some eight or nine miles an hour [14 km/h], preserving its original figure some thirty feet [9 m] long and a foot to a foot and a half [300-450 mm] in height. Its height gradually diminished, and after a chase of one or two miles [2-3 km] I lost it in the windings of the channel. Such, in the month of August 1834, was my first chance interview with that singular and beautiful phenomenon which I have called the Wave of Translation.*

There is no single agreed upon definition of a soliton (see Appendix A). But Drazin & Johnson (1989) [10] describe solitons by its three properties:

1. They are of permanent form;
2. They are localized within a region;

3. They can interact with other solitons, and emerge from the collision unchanged, except for a phase shift.

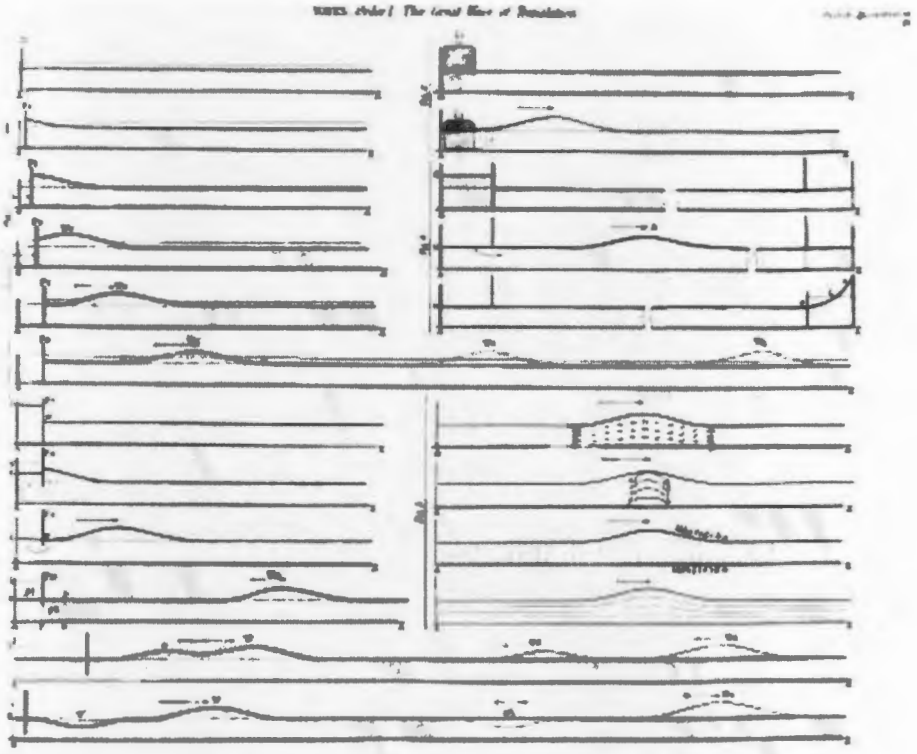

Fig 1.1.1. Following his discovery of a 'wave of translation', Scott Russell built a 30 ft wave tank in his back garden and made further important observations on the properties of the solitary wave. Above are sketches of his wave tank. [25]

In optics, a soliton is any optic field that does not change its shape as it propagates. Usually, this is due to a balance between nonlinear and linear effects in the medium. There are two types of solitons: spatial solitons and temporal solitons.

Spatial solitons, often likened to a graded-index fiber, have electromagnetic fields that change with the refractive index of the medium while propagating. It remains confined and does not change its shape while propagating, by balancing the nonlinear effects with diffraction. Meanwhile temporal solitons, whose electromagnetic field are spatially confined, maintain their shape by balancing nonlinear effects with dispersion.

My experiments will be utilizing spatial solitons. Therefore, any further mention of solitons will specifically be spatial solitons.

1.1.1 Nonlinear Schrodinger-like equation for solitons

For solitons, the nonlinear Schrodinger-like equation with thermal defocusing response [2] included is

$$i\frac{\partial}{\partial z}\varphi + \frac{1}{2k_0 n_b}\nabla_\perp^2\varphi + k_0(n_p - n_b)\rho V\varphi + i\frac{\sigma\rho}{2}\varphi - k_0|\Delta n_T|\varphi = 0,$$

where k_0 is the vacuum wavenumber and $k_0 = \frac{2\pi}{\lambda_0}$, φ is the electric field envelope, $n_{p,b}$ are the refractive indices of the individual particle and background medium respectively, ρ is the intensity dependent particle concentration, V is the volume of an individual particle, σ is the extinction cross section, and Δn_T is the thermally mediated refractive index change of the suspension. Note that Δn_T can be approximated as $\Delta n_T = \left(\frac{\partial n_b}{\partial T}\right)(T - T_b)(1 - f_V)$, where T represents the spatial temperature distribution and T_b is the initial temperature of the suspension.

In this nonlinear Schrodinger-like equation, the first term is the beam propagation evolution, the second term is responsible for diffraction effects, third term is due to optical force-induced nonlinearity (could be Kerr-type or exponential [2, 4]), the fourth term is due to scattering and absorption losses, and the fifth term is due to the thermal defocusing response. In most cases, the thermal defocusing response is considered small and often time ignored (see Appendix B).

1.2 Optical Forces

Contributions to the optical forces that form a soliton are the gradient force, the scattering force, and the absorption force.

1.2.1 Gradient Force

To first order, the underlying gradient force is given by [3, 13, 14, 31, 32]

$$\vec{F}_{\text{grad}} = (1/4)\alpha_{\text{R}}\,\nabla I,$$

where intensity I is given by $I = \vec{E}\cdot\vec{E}^{*}$, $\vec{E}$ is the electric field amplitude, and α_{R} denotes the real part of the particle's polarizability.

Polarizability of Spherical Particles

In a dipole approximation, polarizability of spherical particles is given by [4]

$$\alpha = 3V_P\varepsilon_0 n_b^2\left(\frac{m^2-1}{m^2+2}\right),$$

where volume of the particle V_{P} is approximated by $V_{\text{P}} = \frac{4}{3}\pi a^3$, such that a is the average diameter of the nanosphere, ε_0 is the free space permittivity, n_b is the refractive index of the background medium, and m is a dimensionless parameter $m = \frac{n_P}{n_b}$ that represents the ratio of the particle's index of refraction, n_p, to the index of refraction of the background medium, n_b.

Note that the dimensionless parameter, $m = \frac{n_p}{n_b}$, will determine whether the polarizability is positive or negative. And the polarizability will determine whether the gradient force is either positive or negative. When $n_p > n_b$, our particle polarizability will be positive and the gradient force will act as an attractive force to the particles. Likewise, when $n_p < n_b$, our particle polarizability will be negative and the gradient force will act as a repulsive force to the particles.

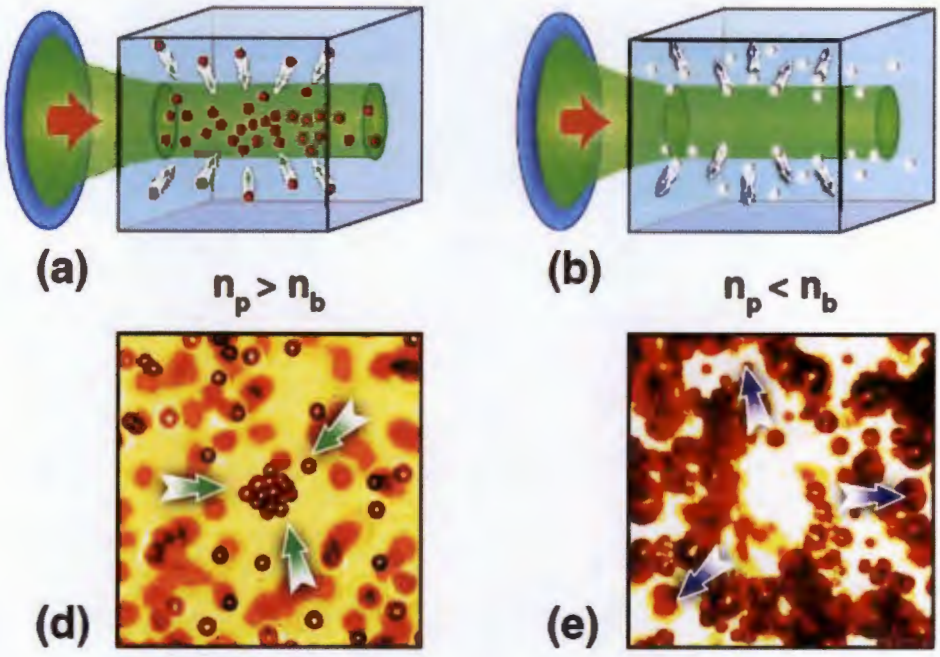

Fig 1.2.1.1. Visual of the gradient force in action. **(a)** and **(d)** When $n_p > n_b$, the particle is positively polarized (PP) and is attracted to the intensity of the beam. **(b)** and **(e)** When $n_p < n_b$, the particle is negatively polarized (NP) and is repelled from the intensity of the beam. [12]

Polarizability of Prolate Spheroidal Particles

Since nanorods do not possess the spherical symmetry, the polarizability of the rod is dependent on orientation. When approximated to be a prolate spheroid, with long semi-axis a and two identical short semi-axes b ($a > b$), the polarizability of a nanorod is [18, 20, 21]

$$\alpha_{||,\perp} = 4\pi ab^2\epsilon_b \frac{\epsilon_p - \epsilon_b}{3\epsilon_b + 3L_{||,\perp}(\epsilon_p - \epsilon_b)}$$

where || and ⊥ denote the rod's longitudinal orientation with respect to the electric field, and ϵ_p and ϵ_b are the frequency-dependent complex dielectric constants of the particle and the background medium. The geometrical structure factor along the longitudinal mode direction is [18]

$$L_{||} = \frac{1-e^2}{e^2}\left(-1 + \frac{1}{2e}\ln\frac{1+e}{1-e}\right)$$

where the eccentricity e is defined as $e^2 = 1 - b^2/a^2$. And the geometrical structure along the short axis is [18]

$$L_{\perp} = \frac{1-L_{||}}{2}$$

1.2.2 Optical Torque

Previous work has shown that in the presence of an electric field, nanorods in plasmonic media have been known to orient themselves [5, 6, 7] along $\vec{E}$ following the optical torque $\vec{\tau} = \vec{P} \times \vec{E}$, where $\vec{P}$ is the polarization and $\vec{E}$ is the electric field.

For nanospheres, due to rotational symmetry, optical torque does not matter. But for my experiments, where nanorods are involved, optical torque is important. Polarizability for my particles will be dependent on orientation. That is to say, when the nanorod is perpendicular to the electric field, the polarizability, $Re(\alpha_{\perp})$, will be different from the polarizability when the nanorod is parallel to the electric field, $Re(\alpha_{||})$.

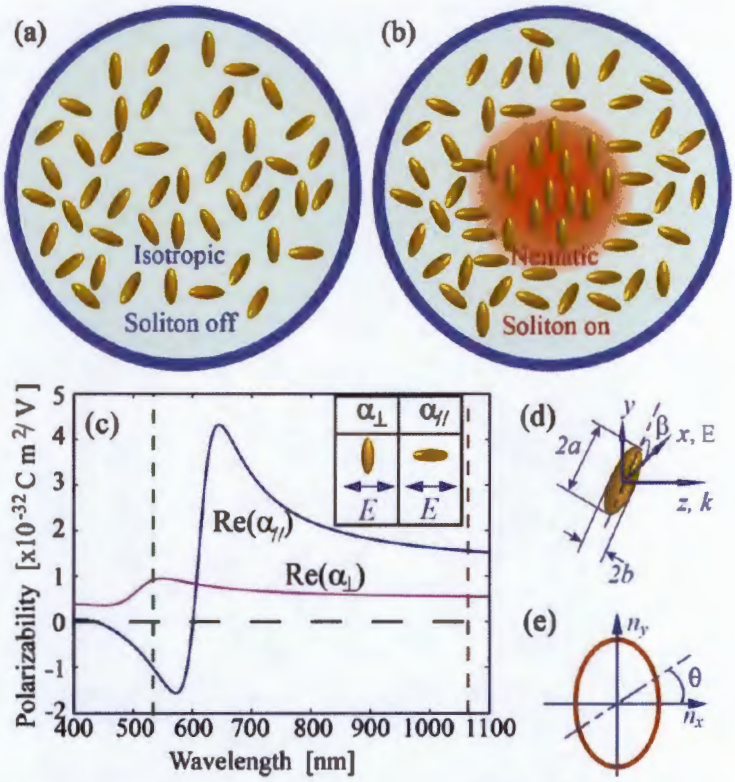

Fig 1.2.2.1. Experimental example of optical torque at work. Gold nanorods encounter optical torque from a linearly polarized pump beam. **(a)** Nanorods have random orientation when no electric field is present. **(b)** Nanorods optically align from optical torque when encountering electric field from a linearly polarized pump beam. **(c)** Plot of polarizability of 100nm nanorods vs wavelength (nm). **(d)** Schematic of gold nanorod. **(e)** Schematic of refractive indices in the orthogonal directions due to induced optical anisotropy. [18]

1.2.3 Scattering Force

The scattering force in optics is analogous to force of radiation pressure ($F_{\text{rad}} = \frac{\sigma}{c}\vec{S}$), such that [31, 32]

$$\vec{F}_{\text{scat}} = n_b \frac{\sigma_{\text{scat}}}{c}\langle\vec{S}\rangle$$

where, σ_{scat} is the scattering cross section, n_b is the refractive index of the background medium, c is the speed of light, and $\vec{S}$ is the Poynting vector.

Scattering Force of Spherical Particles

For spherical particles, $\sigma_{\text{scat}} = \frac{k^4 |\alpha|^2}{4\pi}$ [31]. Recall, in the dipole approximation, the polarizability of a spherical particle is $\alpha = 3V_P \varepsilon_0 n_b^2 \left(\frac{m^2-1}{m^2+2}\right)$. Then the Rayleigh approximated scattering cross section for spherical particles [8] becomes

$$\sigma_{\text{scat}} = \frac{8\pi}{3}\left(\frac{2\pi n_b}{\lambda_0}\right)^4 a^6 \left(\frac{m^2-1}{m^2+2}\right)^2.$$

Note in optics, the time-averaged value of the Poynting vector is the intensity. Also, recall that wavenumber, k, is $k = (2\pi/\lambda) = (2\pi n_b/\lambda_0)$. Thus, our scattering force for spherical particles is (always positive and along z direction):

$$\vec{F}_{\text{scat}} = \frac{8\pi n_b}{3c} k^4 a^6 \left(\frac{m^2-1}{m^2+2}\right)^2 I(\vec{r})\,\hat{z}$$

1.2.3 Absorption Force

The absorption force can be written as [31, 32]

$$\vec{F}_{\text{abs}} = n_b \frac{\sigma_{\text{abs}}}{c} \langle \vec{S} \rangle$$

where σ_{abs} is the absorption cross section, n_b is the refractive index of the background medium, c is the speed of light, and $\vec{S}$ is the Poynting vector.

Absorption Force of Spherical Particles

For spherical particles, $\sigma_{\text{abs}} = k\,\text{Im}(\alpha)$ [31]. Thus, the absorption force for spherical particles is

$$\vec{F}_{abs} = \frac{k\,n_b}{c}\,\text{Im}(\alpha)\,I(\vec{r})\hat{z}$$

1.4 Background of Birefringence

1.4.1 P and S Polarization

A linearly polarized beam of light that is perpendicular to the plane of incidence is known to be s-polarized. The s stands for *senkrecht,* which is German for perpendicular. An s-polarized beam is also known as a transverse electric (TE) mode, since the electric field is perpendicular to the plane of incidence.

A linearly polarized beam of light that is parallel to the plane of incidence is known to be p-polarized. The p stands for *parallel*, which is German for parallel. A p-polarized beam is also known as a transverse magnetic (TM) mode, since the magnetic field is perpendicular to the plane of incidence.

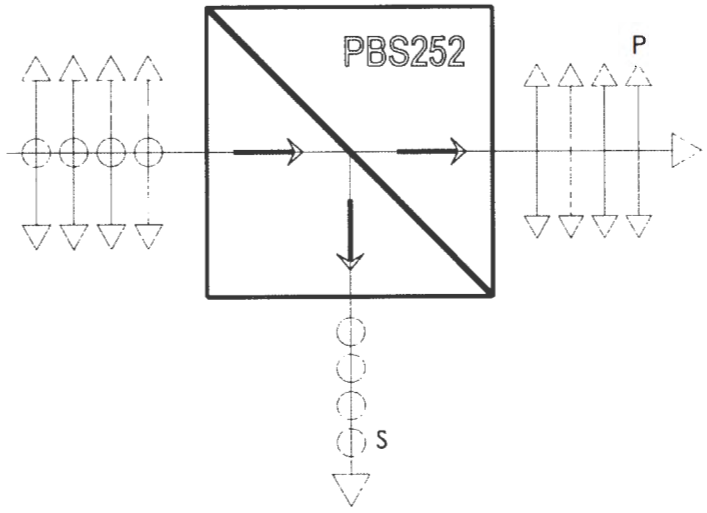

Fig 1.4.1.1. Schematic drawing of a polarized beam splitter (PBS) from Thorlabs, which separates an unpolarized beam into its p-polarized and s-polarized components [40].

1.4.2 Birefringence

Birefringence (also known as double refraction [41]) is the optical property of a material having a refractive index that depends on the polarization and propagation direction of light.

Many anisotropic materials are said to be birefringent or birefractive. Often times, birefringence is quantified by it maximum refractive indices. That is to say, an extraordinary refractive index, n_e, and an ordinary refractive index, n_o.

Some examples of birefringent material are crystals that have non-cubic crystal structures. One common example of a birefringent material is ice. Ice (H_2O) has a hexagonal symmetry and birefringence of $n_e = 1.313$ and $n_o = 1.309$ [9].

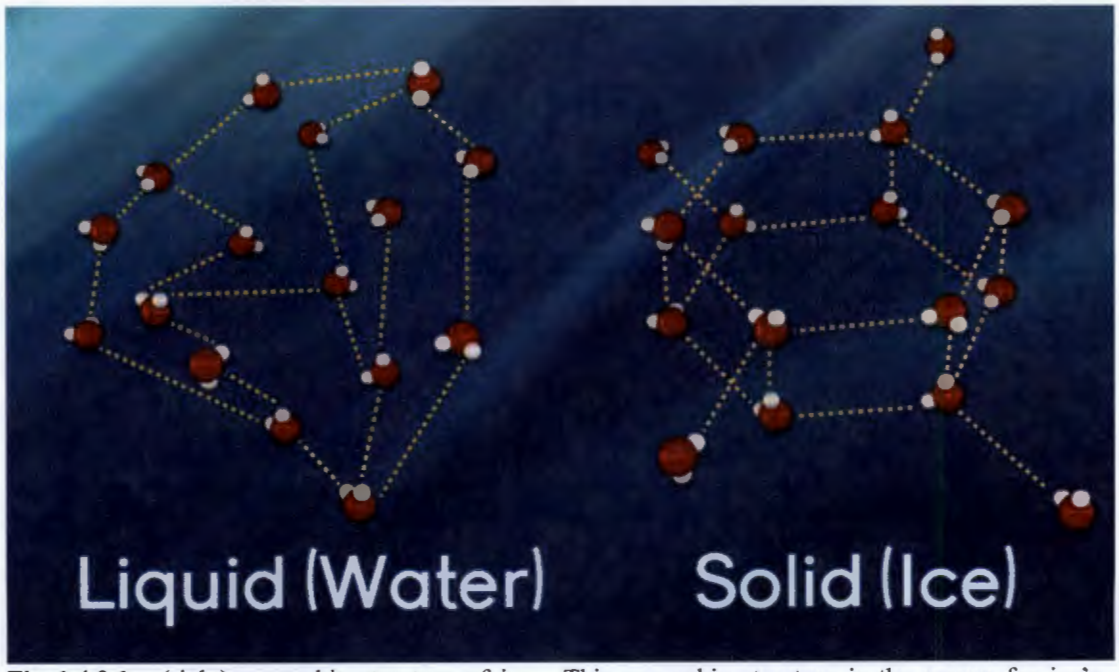

Fig 1.4.2.1. (right) non-cubic structure of ice. This non-cubic structure is the reason for ice's birefringent property. [26]

1.4.3 Birefringent Absorption

Ice (H_2O) is a birefringent dielectric material with ordinary and extraordinary refractive indices that are strictly real [9, 19]. On the other hand, a conductive birefringent colloidal nanosuspension, observed with a soliton beam that is linearly polarized, can exhibit

birefringent absorption [18]. A metamaterial with birefringent absorption (difference in the imaginary part of the refractive index) properties would then have a complex set of extraordinary and ordinary refractive indices: $Re(n_e), Re(n_o), Im(n_e)$, and $Im(n_o)$.

Birefringent absorption is also referred to as dichroism, where dichroism is described by

$$\Delta Im(n) = Im(n_x) - Im(n_y).$$

1.5 Previous Soliton Experiments

I will give a brief description of some relevant soliton experiments. This will not be anywhere near a complete or even brief history. Instead, this will be a short discussion of experiments and papers pertinent to my personal soliton experiments. Most of these experiments were conducted by other past researchers in San Francisco State University. None the less, I feel that I must acknowledge work, for their work led me to mine.

1.5.1 Soliton in Colloidal Suspensions with Mixed Species of Positively Polarizable (PP) and Negative Polarizable (NP) Dielectric Particles

In the field of nonlinear optics, the use of colloidal suspensions and particles with positive polarizability have since long been used [11, 12].

In 2013, Man, *et al.*, used 2μm polystyrene dielectric beads in a deionized water solution. These polystyrene 2μm beads ($n_p = 1.59$) in aqueous colloidal suspension ($n_b = 1.33$) have a positive particle polarizability (PP). Then, Man, *et al.*, demonstrate a new class of synthetic colloidal suspensions with negative particle polarizabilities (NP) [12]. By using hollow 7μm silica spheres ($n_p = 1.2$) in a water solution ($n_b = 1.33$), Man, *et al.*, were able to have a colloidal suspension with NP particles.

With the use of a focused continuous wave (CW) laser beam at 532nm wavelength, and the two aforementioned colloidal suspensions in a 10-mm-long cuvette, Man *et al.*, demonstrated a catastrophic self-focusing collapse with the polystyrene aqueous PP suspension and an enhanced transmission against scattering in the hollow silica aqueous NP suspension. Neither colloidal suspensions yield the desired soliton.

But, by mixing both species (the PP polystyrene beads and the NP hollow silica spheres in water), Man, *et al.*, achieved a mixed response (attraction of PP beads and repulsion of NP spheres due to the gradient force) in their colloidal suspension and were able to realize the creation of a soliton.

By introducing NP particles into a PP environment, Man, *et al.*, were able to alter their colloidal suspension's nonlinear properties and ergo create a stable self-trapping of light [12].

1.5.2 Solitons in Colloidal Nanosuspensions of NP and PP particles

In 2014, Fardad, *et al.*, through the use of plasmonic nanostructures such as core-shell particles, nanorods, and nanospheres were able to display robust propagation of self-trapped light [2]. Fardad, *et al.*, used two kinds of NP particles (gold nanorods, silica-gold core-shells) and two types of PP particles (gold nanospheres, silver nanospheres). And, in all four separate cases, Farad, *et al.*, was able to create solitons [2].

1.5.3 Solitons as Waveguides and Experiments using Nanospheres and Nanorods

In recent years, guiding and steering light has also been observed in colloidal suspensions of dielectric (polystyrene), as well as metallic (silver) nanoparticles [15, 16].

In 2016, Kelly, *et al.*, showed that they can create a plasmonic resonant soliton with colloidal nanosuspensions. This, in turn can be used as a self-induced waveguide [17]. With the use of a focused continuous wave (CW) laser beam at 532nm wavelength, and the colloidal suspensions (gold nanosphere, gold nanorod) in a 4-cm-long cuvette, Kelly *et al.*, created a soliton inside their nanosuspension. Then using this soliton as a waveguide, Kelly, *et al.*, were able to guide a comparably low powered IR beam [17].

1.5.4 Soliton Experiment regarding Birefringence

Now that plasmonic resonant solitons can be used as a wave guide, Ren, *et al.*, used a probe beam (1064nm) to show that a linearly polarized soliton pump beam (532nm) was exhibited orientation ordering in their gold nanorod colloidal plasmonic suspension [18].

Chapter 2: Birefringence/Dichroism Measurements for Aqueous 145nm Gold Rods

With the precedence that plasmonic resonant solitons in aqueous suspensions of gold nanorods can exhibit orientational ordering [18], we attempt to display plasmonic resonant tuning of nanorod orientation, by implementing different pump beam wavelengths for the same aqueous nanorod suspension.

Previously, in the birefringence experiment by Ren, *et al.*, [18] the colloidal suspension used were gold nanorods from NanoPartz [22, 23], whose average length and diameter were 100nm and 50nm, respectively, and whose longitudinal surface plasmon resonance (LSPR) was around 600nm.

It has been shown that the polarizability α_R of gold nanorods in an aqueous solution can be tuned as a function of the rod length when its diameter is fixed at 50nm [2]. By choosing the right set of gold nanorod suspension and pump wavelength we believe we can show that nanorod orientation can be tuned by adjusting wavelength of the linearly polarized pump beam.

2.1. Theory

2.1.1 Polarizability of 145nm Rods, Orientation, and the Gradient Force

We judiciously looked at the available samples from NanoPartz and found an aqueous colloidal suspension whose nonlinear properties could be utilized by our current MSquared continuous wave (CW) tunable laser (λ, 700 to 1000nm).

We chose an aqueous gold nanorod suspension from NanoPartz [22, 24], with an average rod length and diameter of 145nm and 50nm respectively, and an LSPR around 800nm.

We planned on pumping the plasmonic resonant soliton with three different wavelengths: 740, 780, and 840nm. As seen on Fig 2.1.1.1., at these wavelengths, the particle polarizability for perpendicular orientation, $Re(\alpha_{\perp})$, is positive and relatively constant throughout the selected wavelength range. On the other hand, the particle polarizability for parallel orientation, $\mathrm{Re}(\alpha_{||})$, is vastly different for the three wavelengths. For 740nm and 840nm, the magnitude of $\mathrm{Re}(\alpha_{||})$ is comparable, but $\mathrm{Re}(\alpha_{||})$ is negative for 740nm wavelength and positive for 840nm wavelength. While, for 780nm wavelength, $\mathrm{Re}(\alpha_{||})$ has a small positive magnitude by comparison to the magnitudes for 740nm and 840nm wavelengths.

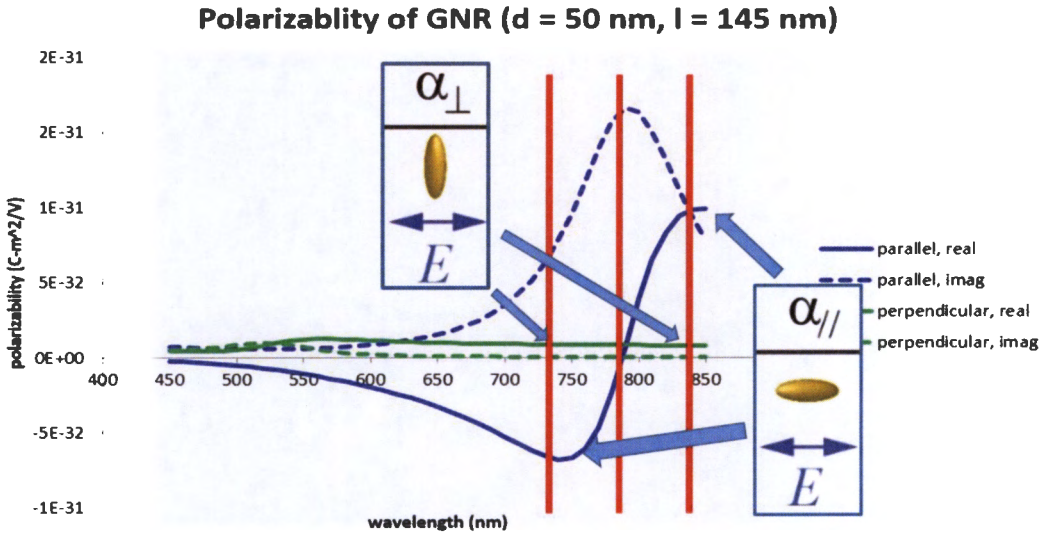

Fig 2.1.1.1. Polarizability (Cm^2/V) vs Wavelength (nm) graph for gold 145nm long rods in aqueous solution. Real and imaginary component are shown for both perpendicular and parallel orientations with respect to the polarization of the pump beam. Red horizontal lines are added to show relative locations for 740, 780, and 840nm wavelengths.

Since $\mathrm{Re}(\alpha_{\perp})$ is relatively constant and positive for our three wavelengths, the effect of the gradient force, $\vec{F}_{\mathrm{grad}} = \frac{1}{4}\alpha_R \nabla |E|^2$, should be relatively the same. That is to say, for all three linearly polarized pump wavelengths (740, 780, 840nm), when the rods are oriented perpendicular to our electric field, the rods should all be transversely attracted to our pump beam. But, when our rods are oriented parallel to our linearly polarized pump beam, we expect different results for the three situations.

For 740nm, since $\mathrm{Re}(\alpha_{||})$ is large in magnitude and negative, the parallel oriented rods should be repelled from the center of the pump beam. This will leave the soliton channel to be largely populated with rods oriented perpendicular to our electric field (Fig 2.1.2(a)).

For 840nm, since $\mathrm{Re}(\alpha_{||})$ is also large in magnitude, but positive, the parallel oriented rods should be attracted towards the center of the pump beam. This will result in a soliton channel that is populated by both parallel and perpendicular oriented rods. But, since $|\mathrm{Re}(\alpha_{||})|_{840}$ is much larger than $|\mathrm{Re}(\alpha_{\perp})|_{840}$, we expect to have majority of the rods in the soliton channel to be oriented parallel to our electric field (Fig 2.1.2(c)).

Finally, for 780nm, since $\mathrm{Re}(\alpha_{||})$ is small in magnitude and positive, a small amount of parallel oriented rods may be attracted towards the center of the pump beam. Furthermore, $|\mathrm{Re}(\alpha_{||})|_{780}$ is much smaller than $|\mathrm{Re}(\alpha_{\perp})|_{780}$, so we expect to have most rods oriented in the perpendicular orientation (Fig 2.1.2(b)).

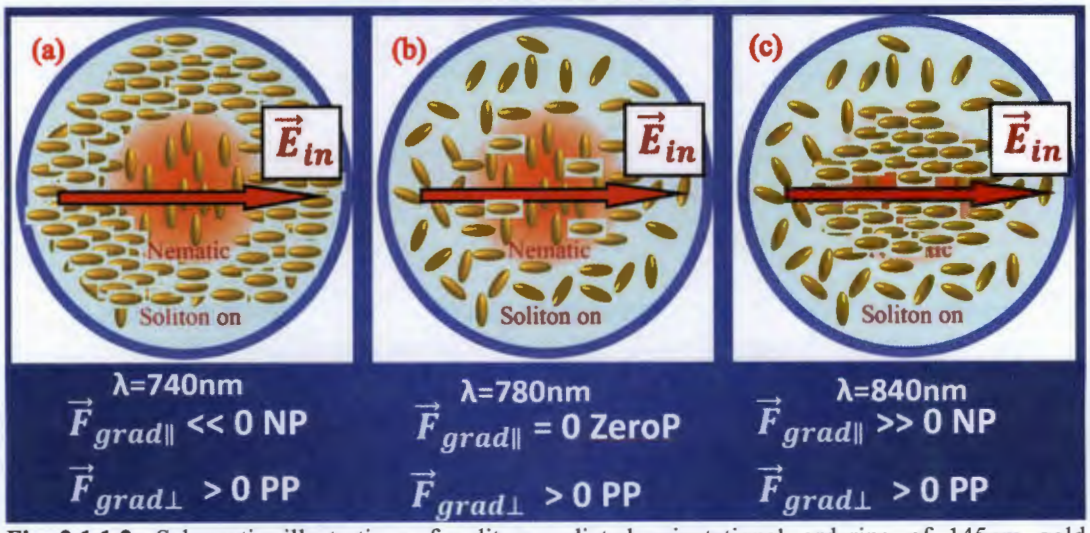

Fig 2.1.1.2. Schematic illustration of soliton-mediated orientational ordering of 145nm gold nanorods at three wavelengths: (a) 740 nm, (b) 780 nm, and (c) 840 nm.

2.1.2 Method for Determining Birefringence and Dichroism

By measuring our pumped soliton beam's birefringent and dichroic properties, we can show that our nanosuspension exhibits ordering when the soliton is present. From experiments [17], we have found that soliton channel can be used as a waveguide for beam that is on the far right of the particle's LSPR. In our case, we will use an IR beam at 1064 nm to probe our soliton channel.

We can further measure the anisotropic properties of this metamaterial by measuring the polarization transmission spectrum of our probe beam linearly polarized at an angle θ_1 with respect to the polarization of the soliton beam (which will be p-polarized, along x-axis).

After the linearly polarized probe beam exits the soliton channel, the output beam generally turns into an elliptically polarized beam.

This can be characterized by measuring the power transmitted through an analyzer placed after the sample as a function of the analyzer's angle θ_2 with respect to the x-axis, given by [47, 48]:

$$\langle |E(\theta_2)|^2 \rangle = I_0 \left[\frac{1}{a} \cos^2\theta_1 \cos^2\theta_2 + a \sin^2\theta_1 \sin^2\theta_2 + \frac{1}{2} \sin 2\theta_2 \cos\delta \right]$$

where

$$I_0 = \frac{1}{2} |E_{in}|^2 \exp\left(-\left(\mathrm{Im}(n_x) - \mathrm{Im}(n_y) \right) k_0 L \right)$$

$$\delta = \left(\mathrm{Re}(n_x) - \mathrm{Re}(n_y) \right) k_0 L$$

$$a = \exp\left(\left(\mathrm{Im}(n_x) - \mathrm{Im}(n_y) \right) k_0 L \right)$$

E_{in} is the input electric field amplitude, n_x and n_y are the indices of refraction along the two principal axes, $k_0 L = \frac{2\pi L}{\lambda}$ is the optical phase that light accumulates when passing through suspension of length L. δ and a describe the induced birefringent and dichroic properties of the metamaterial. (Recall that magnitude of the difference quantified by birefringence is $\Delta\mathrm{Re}(n) = \mathrm{Re}(n_x) - \mathrm{Re}(n_y)$. Similarly, the difference quantified by dichroism is $\Delta\mathrm{Im}(n) = \mathrm{Im}(n_x) - \mathrm{Im}(n_y)$.

If the orientation of the rods is dependent on the wavelength of the pump beam, we expect both the sign and value of $\mathrm{Im}(n_x) - \mathrm{Im}(n_y)$ should change and the major axis of the output probe beam should rotate differently.

2.2 Experimental Setup

The setup used for this experiment is illustrated in Fig 2.2.1, where an MSquared continuous wave (CW) tunable laser (λ, 700 to 1000nm) is used as the pump, while another CW laser operating at an IR wavelength (λ = 1064nm) is used as the probe. Both beams propagate collinearly through a cuvette (2 cm, 4 cm, and 10 cm) containing an aqueous gold nanorod (length = 145nm, diameter = 50nm) suspension.

The pump beam (λ, 700 to 1000nm) passes through an achromatic halfwave plate (690-1200nm) and polarizing beam splitter (620-1000nm) so that the pump beam is linearly p-polarized (TM) and its power can be adjusted. The pump beam is then expanded/collimated before being focused near the input facet (~0.8cm from the front end of the cuvette) of the colloidal suspension in a sample cuvette.

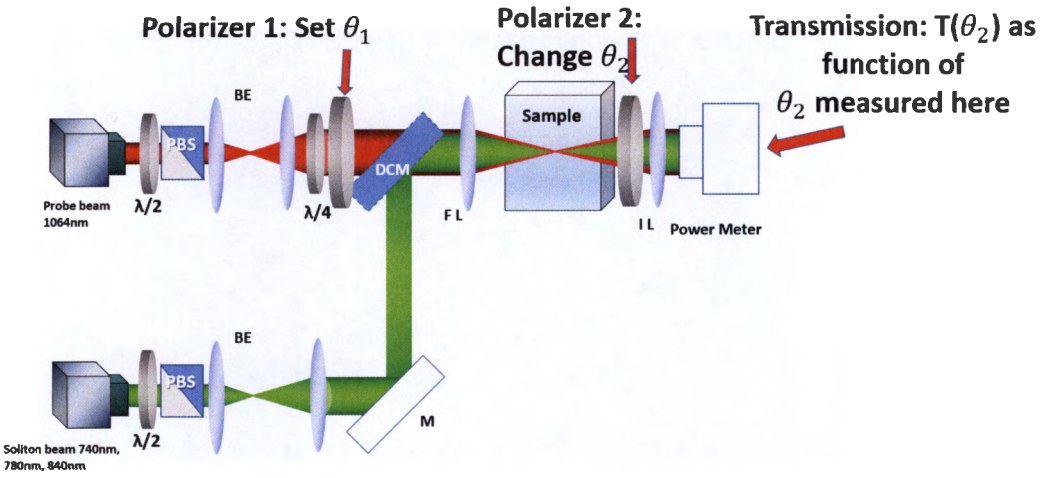

Fig 2.2.1. Schematic of Experimental Setup for Birefringence/Dichroism Measurements.

The probe beam (IR, λ = 1064nm) is also expanded/collimated and passes through a multi-order dual wavelength waveplate (1/2-wave at 1064nm & 1/4-wave at 532nm) and

polarizing beam splitter (900 -1300nm) so that it is also linearly p-polarized (TM) and its power can also be adjusted. The probe beam then goes through multi-order dual wavelength plate (1/2-wave at 532nm & 1/4-wave at 1064nm) at 45 degrees with respect to the p-polarization to create a relatively circularly polarized beam. After the quarter-wave plate, the probe beam then goes through an ultra broadband wired grid polarizer (250 – 4000nm) and emerges as a linearly polarized beam.

The pump beam and probe beam get combined through a long pass dichroic mirror (950nm cutoff wavelength) before being focused together by an achromatic lens with a focal length of 80mm. The diameters of the collimated pump and probe beams are 5.0 and 6.5 cm, respectively, and the corresponding beam sizes at the focal plane are measured to be 21.4 and 16.6 μm respectively.

The input and output beam profiles are monitored by a CCD camera (Thorlabs, UBS 2.0) and series/combination of neutral density (ND) filter camera caps and ND wheels. The input/output power is measured using a power meter (Thorlabs, PM100D) along with either a photodiode sensor (Thorlabs, S130C) or a thermal power sensor (S302C). The power of the output probe beam after the sample is then measured with or without the analyzer placed after the sample.

2.3 Results/Discussion

Expectations

With the analyzer, we measure the output at θ_2 from 0 to 2π. When the soliton pump was not on, we expected to see the IR probe output follow Malus's law [18], such that the output intensity behaves as $I = I_0 \cos^2(\theta_2 - \theta_1)$, where θ_2 is the angle of the analyzer with respect to the polarization of the pump beam, and θ_1 is the angle of the linearly polarized input probe with respect to the polarization of the pump beam.

We will measure the transmitted power as a function of θ_2. If there is no difference in the real and imaginary refractive indices, our transmission should follow Malus's law and the minimum transmitted power should be at about 0mW.

For the 740nm wavelength, we expect the rods to be oriented perpendicular to the soliton's electric field. This will cause a difference in the imaginary refractive indices, indicating dichroism [47, 48]. As a result, the peak position should shift to the left.

For the 840nm wavelength, we expect many rods oriented parallel to the soliton's electric field [47, 48]. This will cause a difference in the imaginary refractive indices. And as a result, the peak position will shift to the right.

Results

Data for the experiment (Fig 2.3.1) was taken in the span of about nine hours. The input probe beam with a power of about 5mW was linearly polarized at $-10°$ and verified to have an extinction ratio of $362:1$. The transmission of the probe beam when the soliton was off was about 11%.

At the local max, the 840nm pumped soliton was measured to have an increase in probe power by 1.2 times. While 780nm and 740nm pumped solitons had an increase of 1.28 and 1.36 times respectively. The increase in the modulation amplitude from the off-to-on transition by the soliton occurred as expected [18].

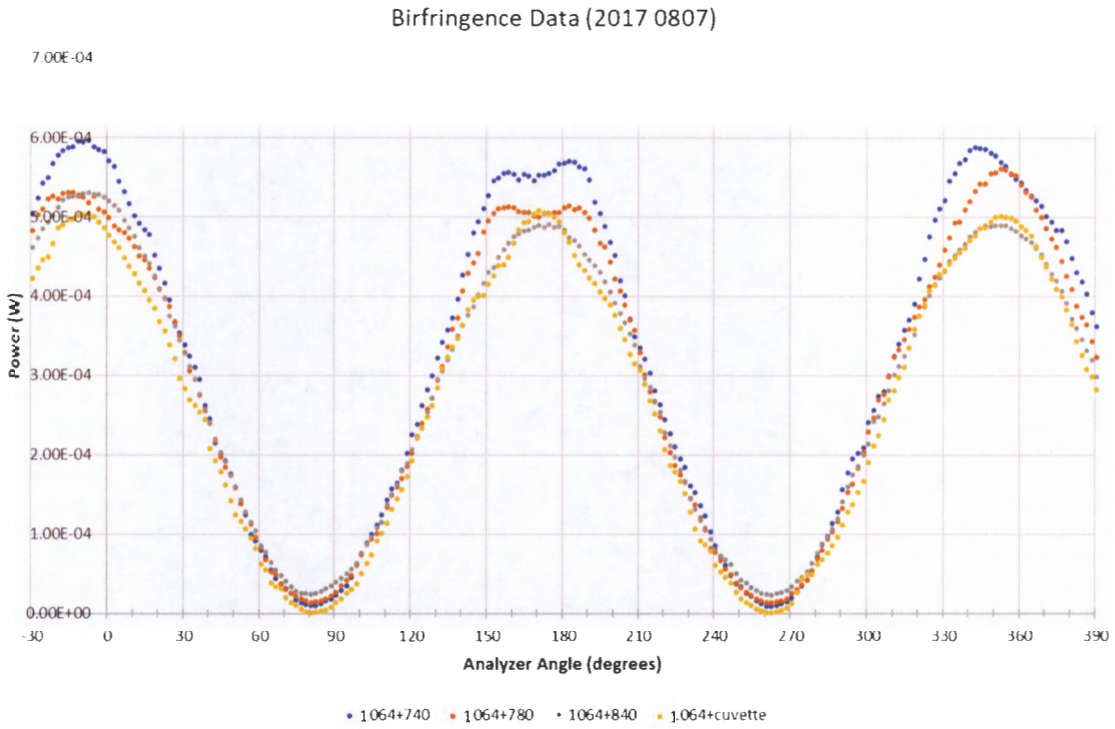

Fig 2.3.1. Birefringence results. The x-axis is the angle of θ_2 (degrees) and the y-axis is the measured power output (W). The input probe (1064) was set to 5mW at $\theta_1 = -10°$. The output was then measured at θ_2 ranging from $-10°$ to 390° with 2° increments for soliton pumps 740nm, 780nm, and 840nm. All soliton pump beams were linearly polarized at 0°. The soliton pump powers were about 630mW, 612mW, and 610mW, respectively.

When the pump was off ('1064+cuvette'), the output has peaks (Fig 2.3.2) at $-10°$, 170°, and 350°, as expected, and minimums at (Fig 2.3.3) about 80° and 260°, as expected. Futhermore, the minima follow Malus's Law and are at about 0mW.

But the direction of the phase shifts (Fig 2.3.2) was not as expected. Furthermore, the phase shifts were inconsistent within the three peaks. Note the inconsistencies between the first and third peaks in Fig 2.3.2. Also note that for '1064+740' and '1064+780', there does not seem to be a second peak. These results suggest that there is some systematic fluctuation in our systems.

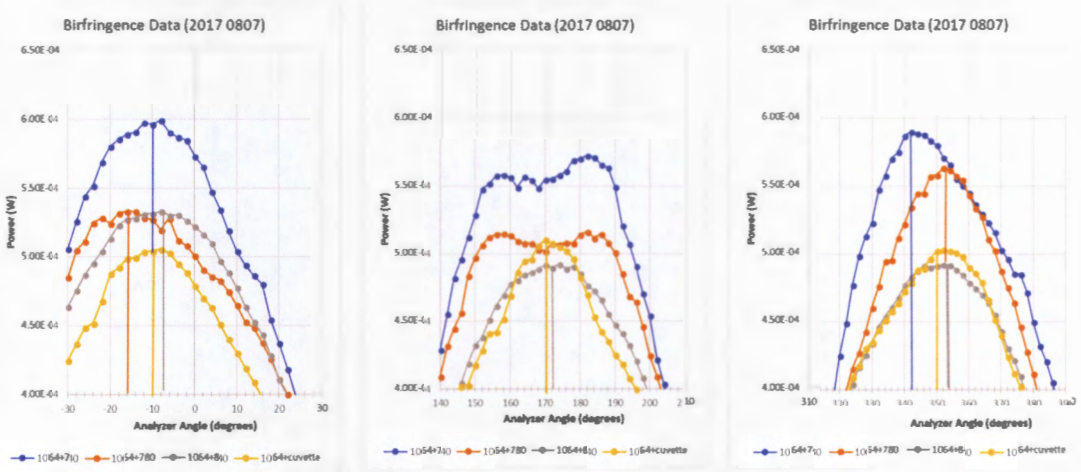

Fig 2.3.2. Close-up views of the three peaks from the Birefringence data results from 2017 0807. Orange, yellow, and gray vertical lines were added to show the estimated peaks of the outputs with respect to the peak of the input (blue). We see the phase shifts were very small and inconsistent within the three peaks.

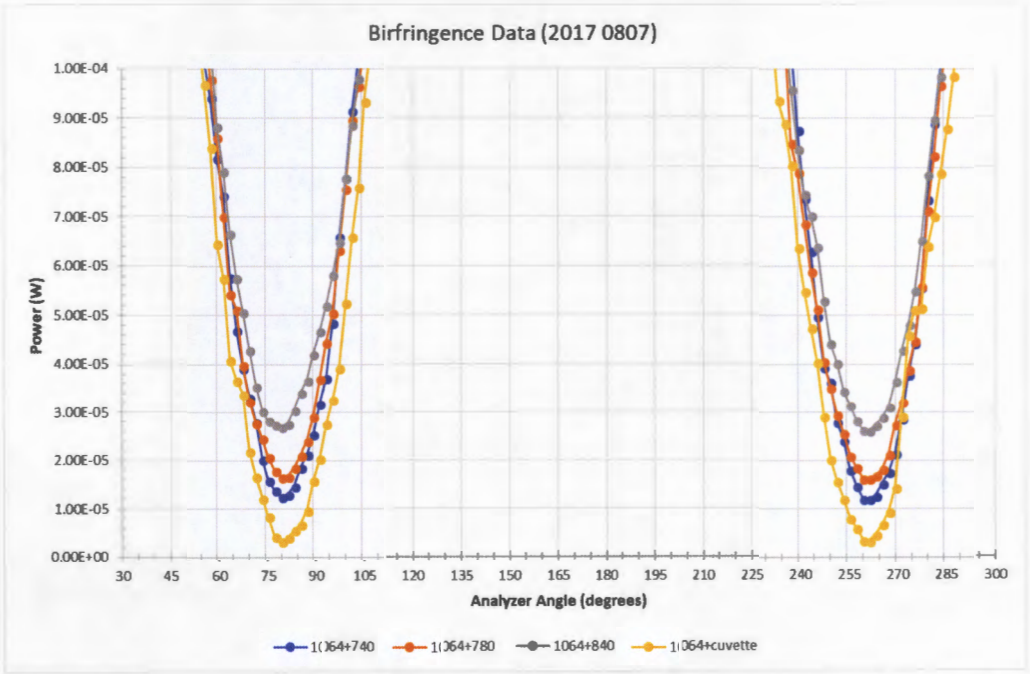

Fig 2.3.3. Close-up views of the two minima from the Birefringence data results from 2017 0807. The IR probe output ('1064+cuvette') follows Malus's Law and has a minimum of about 0mW, as expected. Furthermore, the pumped outputs ('1064+740', '1064+780', and '1064+840') have minima slightly about 0mW (about 0.1mW to 0.3mW). This slight increase is due to the Birefringent/Dichroic effect of the nanorods being ordered.

Discussion

It should be reiterated that the data was taken over the span of nine hours. And although negligible, the non-linear Schrodinger-like equation for solitons [2] still has thermal effects. It can be seen in the soliton's sinking feature that we often dismiss (see Appendix B). If that is truly the case, then nine hours of being exposed to high powered electric fields from the laser beam could cause some small amounts of evaporation to our sample. Therefore, one explanation for inconsistency could be the change in the sample particle concentration over time.

It should also be noted that from previous work with 100-nm-long nanorods [18], the phase shift was found to be at about 1°, indicating a very small Birefringence difference between ordinary and extraordinary refractive indices.

This experiment was repeated several times. The results were inconsistent. System error was vastly considered. To reduce the time of measurement, we purchased a servo operated step motor to rotate the analyzer and reduce the data acquisition time. Unfortunately, our results were still not as "expected" due to limited propagation distance and the subtle difference which cannot be effectively resolved within experimental errors [47]. We eventually explored another experiment that is designed to obtain nanorod ordering by applying an external electric field. Based on results from this experiment (Chapter 3.2), we re-visited the birefringence/dichroism experiment, but used an organic (toluene) solution (Chapter 4).

Chapter 3:
Ordering Rods using a High Voltage Applied External Field

Controlling the orientation of nanorods can be done by the use of a high voltage source applied to a pair of parallel conducting plates between a nanosuspension [34, 35, 39]. By using an external electric field and measuring the transmission spectrum of a white light source, the absorption spectrum of the nanosuspension can be obtained.

The alignment of long (aspect ratio > 10) nanorods in aqueous solvents using an external electric field, where only the transverse absorption peak was in the visible spectrum, has been demonstrated with an AC voltage source (25, 125, or 175V) at a high frequency (100 kHz) [34]. For shorter (aspect ratio < 10) nanorods in an aqueous solution, it was known to be difficult and challenging to order the rods using an external electric field.

But recent work has shown that it is possible to align gold nanorods with smaller aspect ratios when in an organic solvent, using an AC voltage source (ranging from 0 to 15kV) at a low frequency (60Hz), gold nanorods in a toluene solvent can be aligned [35, 39].

3.1 Experimental Setup and Theory

The setup used in this experiment is illustrated in Fig 3.1.1, where we used an Ocean Optics (HL-2000) white light source (λ, 400nm—1000nm). We then used a neutral density filter to attenuate power and an ultra broadband wire grid polarizer (250 – 4000nm) to set the white light to p-polarized (0°) or s-polarized (90°).

The linearly polarized white light source was then expanded/collimated and passed through a focusing lens with a focal length of 65mm. The white light was focused near the input facet (0.2cm from the front end) of the colloidal suspension in a sample cuvette (l =12.50mm).

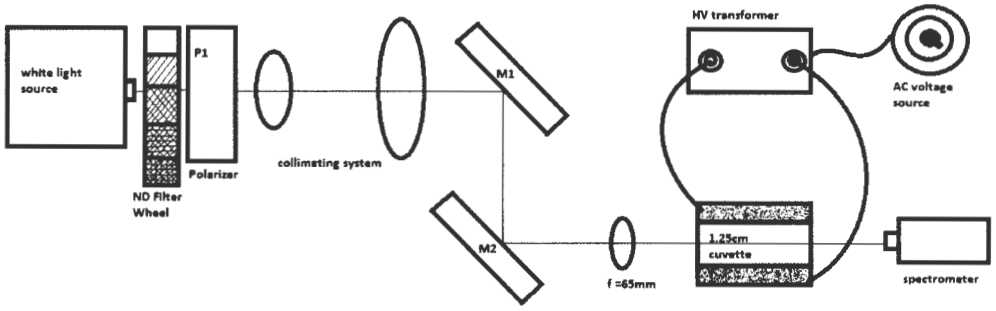

Fig 3.1.1. Illustration of setup for high voltage applied electric field experiment.

A pair of small metal plates (26mm x 13mm) was placed outside the sample cuvette and arranged to only overlap between the cuvette. The plates were connected to high voltage wire cables (Allied Wire & Cable, 3239-14-15KV-9) and were fused together using a silver conductive epoxy (MG Chemical, #8331-14G). These plates were then glued inside a set of 4-cm-long cuvettes using a UV activated glue (5 Second Fix™). These 4-cm-long cuvettes were then filled with Dow Corning Silicon Fluid (Part # PMX200GL10B), which was used as a dielectric fluid to avoid arcing from our high voltage (up to 15kV AC) powered metal plates.

To power the high voltage plates, we had a variable AC voltage source whose output ranges from 0 to 120V at 60Hz. This voltage source was then connected to a FranceFormer transformer with primary at 120V and secondary at 15kV, rated at 60Hz and 30mA.

The distance of our electric plates was about 11.6mm, which gave us an applied uniform electric field that could range from 0 to 1.29kV/mm. When the high voltage plates are activated the nanorods should tend to align along the direction of the external electric field (0°).

After the white light passes through our 12.5-mm-long cuvette, we measure the output spectrum using a Thorlabs compact spectrometer (CCS200) in the wavelength range from 200 to 1000nm with a resolution of $\Delta\lambda < 2$nm and a slit width of 20μm.

Note that the parallel plates are aligned along the vertical direction, which is perpendicular to the propagation direction of the white light source. Thus, when our polarizer is set to 0° and our high voltage plates are activated, our rods should be oriented parallel to the polarization of white light and $\mathrm{Re}(\alpha_{||})$ should dominate. On the other

hand, when our polarizer is set to 90° and our high voltage plates are activated, our rods should be oriented perpendicular to the polarization of the white light and $\mathrm{Re}(\alpha_{\perp})$ should dominate.

For this experiment we tried several samples of nanorods with varying concentrations. For the aqueous solutions, we tried four species of nanorods, all from NanoPartz [22], with varying concentrations: A12-50-60-CTAB [23], A12-50-800-CTAB [24], A12-2100-CTAB [43], A12-25-1400-CTAB [44]. As for the organic solutions, we tried two versions of the same species of nanorods from NanoPartz [45] (the difference being the ligand change from Polystyrene to NanoPartz Organic™), with varying concentrations: E12-50-800-PS-TOL-50 and E12-50-800-NPO-TOL-50.

3.2 Results and Discussion

Results for Aqueous Solutions

Based on a series of experimental test, we could not get any reasonable results with our aqueous solutions to signify that out rods were being ordered by the applied external field. We were not surprised by this with two of our samples: the 100nm long nanorods (A12-50-600-CTAB) and the 145nm long nanorods (A12-50-800-CTAB) because their aspect ratios were much less than 10 (Table 3.2.1). All previous experiments [34] have shown that it is difficult to align nanorods of small aspect ratios in an aqueous solution using an applied electric field, possibly due to an optical torque that is too weak to overcome strong Brownian motion of the nanorods.

On the other hand, we were expecting to get reasonable ordering results from of two large aspect ratio rods (A12-10-2100-CTAB and A12-25-1400-CTAB). In particular, we were expecting to get noticeable ordering results for A12-10-2100-CTAB, since its aspect ratio is 20.8. Ordering with nanorods in an aqueous solution has been done before by van de Zande, *et al.* [34]. We compared our sample characteristics (Table 3.2.1) with the sample characteristics in previously reported experiments (Table 3.2.2).

	L/d	L (nm)	d (nm)	C_{AU} (μg/mL)	C_{RODS} (10^{10}/mL)
A12-10-2100-CTAB	20.8	250	12	35	6.41
A12-25-1400-CTAB	10.2	256	25	50	2.06
A12-50-600-CTAB	2.0	100	50	50	1.32
A12-50-800-CTAB	2.9	145	50	55	1.00

Table 3.2.1. Characteristics of our gold nanorod aqueous solutions from NanoPartz. L/d is the aspect ratio where L, d is the average length and diameter of the nanorods, determined by TEM analysis. C_{AU} is the total gold concentration, determined by ICP optical emission spectroscopy. C_{RODS} is the number concentration of rods, calculated using the previous information provided by NanoPartz.

Note that the information above was given to us by NanoPartz, with the exception of the number concentration of rods, C_{RODS}, which was calculated using the following equation [34]

$$C_{RODS} = \frac{C_{AU}}{\rho_{AU}\pi r^2 L}$$

where the mass density of gold, $\rho_{AU} = 19.3 \times 10^3\ kg\ m^{-3}$.

	L/d	L (nm)	d (nm)	C_{AU} (μg/mL)	C_{RODS} (10^{10}/mL)
ROD2.6	2.6	39	15	30	20
ROD12.6	12.6	189	15	131	20
ROD17.4	17.4	279	16	28	2.9
ROD49	49	729	15	145	2.8
ROD17.2	17.2	259	15	24	2.7

Table 3.2.2. Characteristics of gold nanorod aqueous solutions from van de Zande's [34] experiments, which were successful in showing ordering with long aspect ratio nanorods in aqueous solutions.

Comparing the nanorod characteristics shown in the above two tables, one can see that the rod concentration for our samples is somewhat much less than some of van de Zande, *et al.*'s samples [34]. So we tried concentrating our nanorods samples by using a centrifuge to separate the rods from DI water, and then removed some of the DI water to increase nanorod concentration. We were still unsuccessful. (We later realized, after getting successful results with our organic toluene solution, that Zande, *et al.* used a high

frequency (100kHz) high voltage AC signal. We, on the other hand, were using a low frequency (60Hz) high voltage AC signal. Therefore, using a high frequency high voltage AC signal may be the key to achieving alignment of large aspect ratio rods in an aqueous solution.)

Results for Organic (toluene) Solutions

For the organic nanorod solution, we used toluene as a solvent because previous experiments found success in ordering rods in toluene [35, 39]. We purchased nanorod samples from NanoPartz [45] (E12-50-800-PS-TOL-50 and E12-50-800-NPO-TOL-50) with the same nanorod dimensions (average diameter of 50 nm and average length of 145 nm) as our aqueous nanorod sample in our Birefringence/Dichroism experiment.

This sample from NanoPartz came highly concentrated with optical density (OD) at 50. In fact, it was so concentrated that none of the white light could transmit through the sample, due to the very large absorption from the rods. So, we slowly added toluene (0.300mL at a time) to our sample until we found a sample-to-toluene ratio (0.05mL sample:1.00mL toluene) that could transmit a reasonable percent of our white light spectrum and still be ordered by our applied electric field.

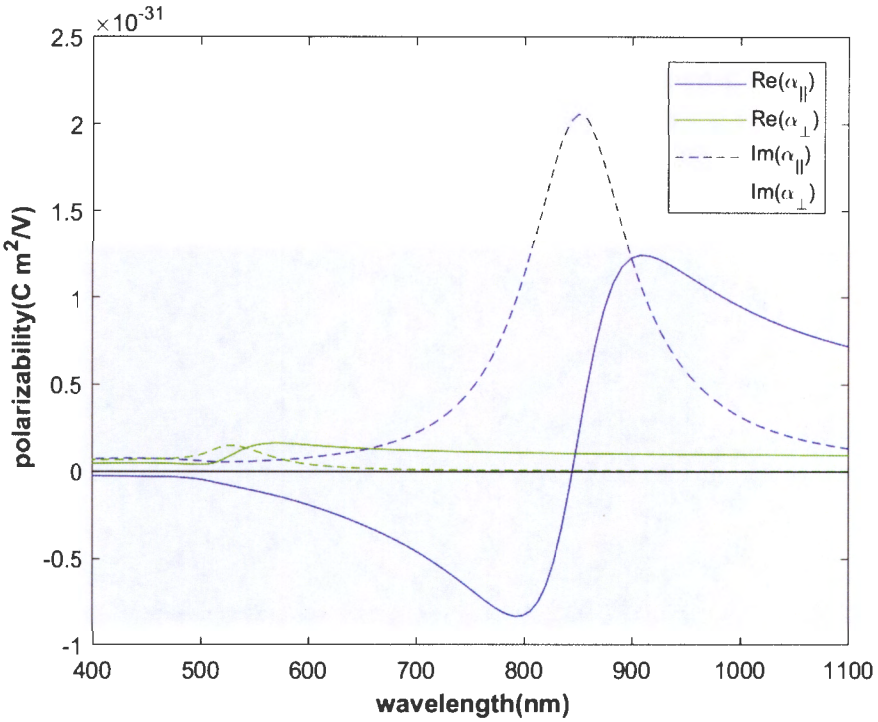

Fig 3.2.1. Real and imaginary $\alpha_{\perp}$ and $\alpha_{||}$ vs wavelength for a nanorod sample ($d = 50$nm, $l = 145$nm) in toluene solvent. This data was numerically calculated using COMSOL.

When the external electric field is applied, our nanorods will tend to orient along the direction of the applied electric field. The higher the electric field, the more nanorods we expect to align themselves along the direction of the electric field.

Our nanorod sample (E12-50-800) has longitudinal surface plasmon resonance (LSPR) at around 860 nm and a transverse surface plasmon resonance (TSPR) at about 550nm (Fig 3.2.1). We can also observe the two resonances by measuring the absorption spectrum when there is no applied electric field (Fig 3.2.2.).

When our polarizer, P1, is set to 0°, more rods will be parallel to the linear polarization of our white light source. Thus, $\mathrm{Im}(\alpha_{||})$ will dominate and the absorption peak around the LSPR (860nm) should increase as the strength of the applied electric field increases. Meanwhile, our absorption peak around the TSPR (550nm) should decrease as the strength of applied electric field increases (Fig 3.2.2).

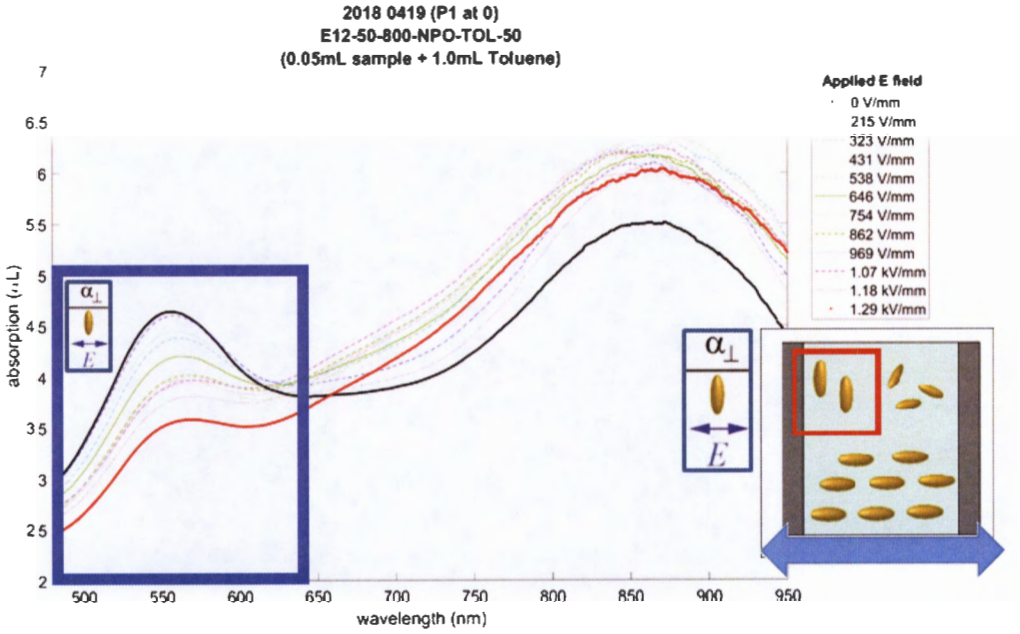

Fig 3.2.2. Absorption (αL) vs wavelength (nm) of organic (toluene) nanorod solution when the linearly polarized white light is parallel to the applied electric field. LSPR is around 860nm and TSPR is around 550nm. A smoothing function involving a moving average was applied to the raw data.

When our polarizer, P1, is set to 90°, more rods will be perpendicular to the linear polarization of our white light source. Thus, Im($\alpha_\perp$) will dominate and the absorption peak around the LSPR (860nm) should decrease with increasing applied electric field. Meanwhile, our absorption peak around our TSPR (550nm) should increase with increasing applied electric field (Fig 3.2.3).

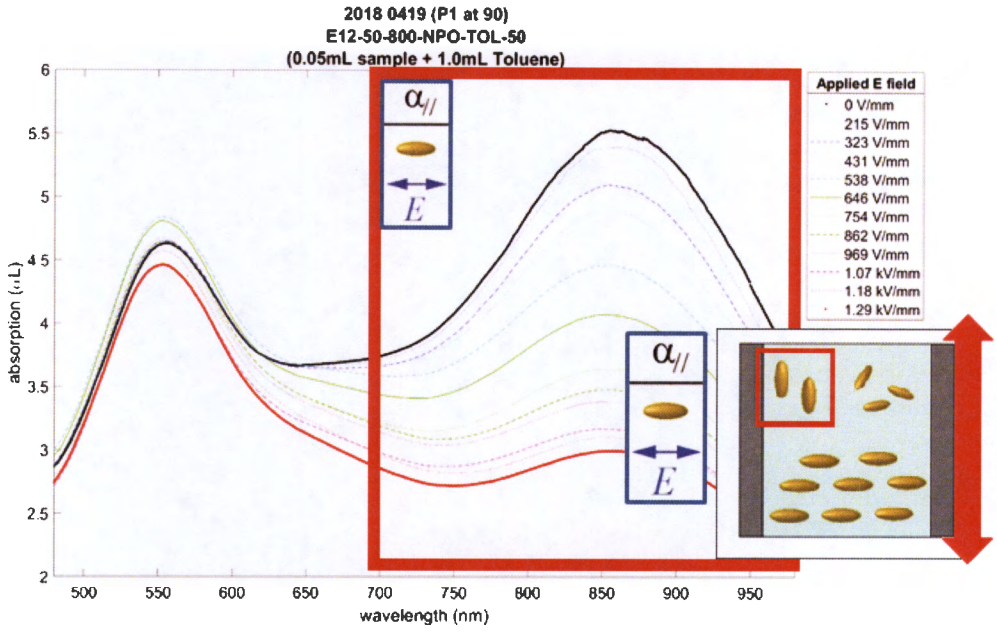

Fig 3.2.3. Absorption (αL) vs wavelength (nm) of organic (toluene) nanorod solution when the linearly polarized white light is perpendicular to the applied electric field. LSPR is around 860nm and TSPR is around 550nm. A smoothing function involving a moving average was applied to the raw data.

From Fig 3.2.2, we see that the decrease in absorption around 550nm is very clear and correlates with the increase in the applied electric field from the high voltage plates. While the increase in absorption around 860nm looks somewhat inconsistent with our expectations. Similarly, from Fig 3.2.3, we see that the decrease in absorption around 860nm is very clear. While the change in absorption around 550nm with applied electric field is again more complex. Upon closer inspection, we find that the inconsistency starts when the applied electric field is greater than 538 V/mm. We suspect something other than just ordering may be happening when the applied electric field is very large. Or, there may be some systematic error for the applied electric field above 538 V/mm.

We took the data from Fig 3.2.2 and Fig 3.2.3 and plotted them on one graph, for a range of applied electric field from 0 to 538 V/mm.

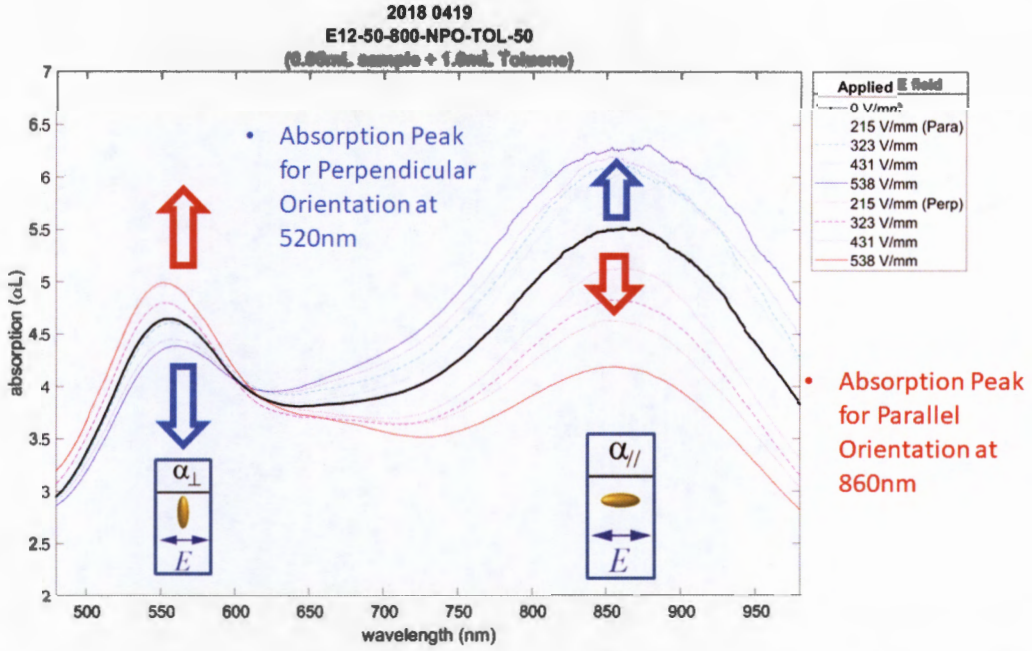

Fig 3.2.4. Absorption (αL) vs wavelength (nm) of organic (toluene) nanorod solution when the linearly polarized white light is either parallel or perpendicular to the applied electric field. LSPR is around 860nm and TSPR is around 550nm. A smoothing function involving a moving average was applied to the raw data.

Fig 3.2.4 shows the absorption vs wavelength of our nanorod in toluene solution when both P1 = 0° and P1 = 90° are included and the applied electric field ranges from 0 to 538 V/mm. The blue/cyan dotted lines represent when the light is linearly polarized at 0° and high voltage is applied to the parallel plates. The red/magenta solid lines represent when the white light is linearly polarized at 90° and high voltage is applied to the parallel plates. The black line denotes the absorption spectrum when no high voltage is applied, and therefore the solution is isotropic.

Note that our nanorod in toluene solution has the same dimensions ($d = 50$nm, $l = 145$nm) as our nanorod in water solution from chapter 2. Therefore, our nanorod in toluene solution will have similar polarizability characteristics as Fig 2.1.1.1. From the black curves in Fig 3.2.2, Fig 3.2.3, and Fig 3.2.4, we can see for nanorods in toluene the absorption spectrum exhibits peaks at 550nm and 860nm. Therefore, we can infer that $\mathrm{Im}(\alpha_{||})$ has an LSPR at about 860nm and $\mathrm{Im}(\alpha_{\perp})$ has a TSPR at about 550nm. Further, we can infer that $\mathrm{Re}(\alpha_{||})$ is negative below 860m and positive above 860nm.

From the blue/cyan dotted lines in Fig 3.2.4, we see a decrease in absorption around 550nm as the high voltage increases and we see an increase in absorption around 860nm as the high voltage increases. We've assumed that the high voltage is aligning more and more of the rods parallel to the linear polarization of white light (P1=0°). Now, with the decrease around $\mathrm{Im}(\alpha_{\perp})$ and increase around $\mathrm{Im}(\alpha_{||})$, we can see that the rods are truly being ordered along the uniform applied electric field.

This idea of ordering from an applied electric field was further confirmed by the results for a different linear polarization of white light (P1=90°, red/magenta solid lines in Fig 3.2.4). We can see an increase in absorption around 550nm and a decrease in absorption around 860nm as the high voltage increases.

Discussion

With this experiment we see that we can order the nanorods in toluene using an applied high AC voltage at low frequency. We found difficultly in ordering nanorods in DI water using the same setup. One explanation could be due to the dipole nature of water. Since water is a polar molecule, our electric field may also be interacting with the water molecules as well as the nanorods, affecting the Brownian motion. In Chapter 2, we also found difficulty in the demonstration of nanorod ordering in aqueous suspension with solitons induced by a pump laser at various wavelengths. This prompted us to try and repeat the Chapter 2 experiment with nanorods in toluene solution.

Chapter 4:
Dichroic Measurements for 145nm Gold Rods in Organic Solvent

In Chapter 2, we attempted measuring the birefringence and dichroism of our soliton induced gold nanorod suspension in an aqueous solution. We found our results to be inconclusive. In Chapter 3, we explore ordering nanorods in a suspension using an external electric field. We found that it is possible to align nanorods in toluene but difficult to do so for a nanorod suspension in water. Thus, we wanted to explore measuring the dichroism of a nanorod suspension in toluene.

4.1 Theory

This experiment used the similar setup as the experiment in chapter 2 (Fig 2.2.1), except the analyzer (θ_2) was removed.

By removing the analyzer placed after the sample, we can now measure the total output power of the probe beam for a given polarization θ_1 of the input probe beam [48]:

$$\langle |E|^2 \rangle = \frac{1}{2} |E_{in}|^2 \left[exp(-2\mathrm{Im}(n_x) k_0 L) \cos^2 \theta_1 + exp\left(-2\mathrm{Im}\left(n_y\right) k_0 L\right) \sin^2 \theta_1 \right]$$

Thus, by measuring the total transmission, T, of the probe beam at $\theta_1 = 0°$ and $90°$, we will be able to obtain the dichroic property, $\Delta\mathrm{Im}(n) = \mathrm{Im}(n_x) - \mathrm{Im}\left(n_y\right)$, of the synthetic material:

$$a = \exp\left(\left(\mathrm{Im}(n_x) - \mathrm{Im}\left(n_y\right)\right) k_0 L\right) = \sqrt{\frac{T(90°)}{T(0°)}}$$

4.2 Experimental Setup

The experimental setup is similar to that used in the experiment described in chapter 2 (Fig 2.2.1) but some changes have been made. The setup used for this experiment is illustrated in Fig 4.2.1.

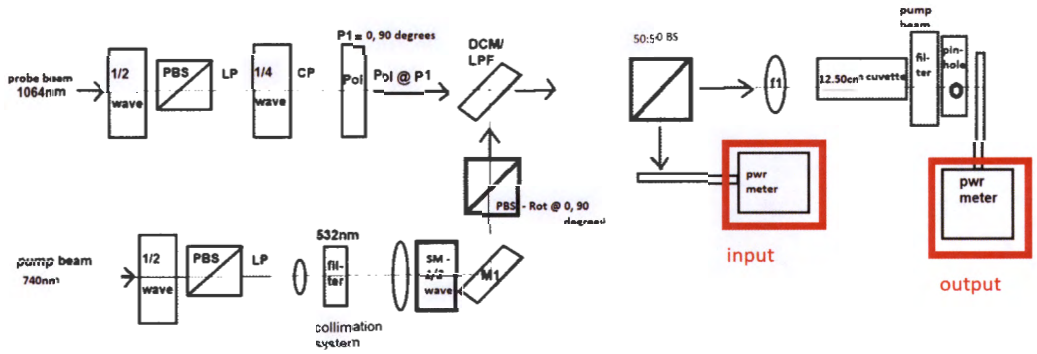

Fig 4.2.1. Schematic drawing of the setup for dichroism experiment with nanorod ($d = 50\text{nm}, l = 145\text{nm}$) suspension in toluene solution.

The collimated probe beam (1064nm) path has a halfwave plate and polarized beam splitter (PBS) which will attenuate the probe beam power and give us an p-polarized probe beam. After that, we have a quarter wave plate at 45° to obtain a circularly polarized probe beam. We then use a polarizer to linearly polarize our beam to an angle of our choice.

The pump beam (740nm) path has a halfwave plate and PBS which will also attenuate the pump beam power and give us a p-polarized pump beam. Then the pump beam is also collimated so that the beam sizes of the pump and the probe are similar. We have a 532nm filter to filter out any residual 532nm beam from the MSquared laser. Then we added another set of halfwave plate and polarized beam splitter. The second halfwave plate is attached to a servo control motorized step motor. And the second PBS is attached to a fixture that can rotate, so that the pump beam can be alternated between p-polarized (0°) and s-polarized (90°).

With the second set of half-wave plate and PBS, we can take data for a decent range of input pump power.

The pump beam (740nm) and probe beam (1064nm) then meet at a dichroic mirror such that their paths line up. Due to the restrictions of our dichroic mirror (see Appendix C),

the polarization of our probe beam will be limited to either P1 = 0° or P1 = 90°, because for other angles the probe beam starts to become elliptically polarized.

For this experiment, we wanted to measure the input pump power and the output probe power at same time. In order to do this, we added a 50:50 beam splitter before our focusing lens (focal length 80mm) and 12.5cm sample cuvette. This way we could measure the input power of the pump beam using a photodiode operated power meter. After the sample cuvette, we added a long pass filter to filter out the pump beam, so that we can only measure the transmission of the probe beam. And then we added a pinhole to block out any residual optic noise. Finally, we use a second photodiode operated power meter to measure the output probe transmission.

4.3 Results

Dichroism Results

We took several rounds of data. When the pump beam was linearly polarized at 0°, we measured the dependence of probe output power on pump power for P1 at 0° and then for P1 at 90°. This measurement was repeated three times. We then took another three rounds of data when the pump beam was linearly polarized at 90°. For all six sets of data, the input pump power and the output probe transmission were measured simultaneously using two separate photodiode operated power meters that were connected to two separate computers.

To attenuate the input pump power, we had automation script to rotate our half-wave plate from minimum power (45°) to maximum power (0°) at a 1° decrement every 2.5 seconds. Using another automation program, we simultaneously recorded the input pump power and output probe transmission every 2.5 seconds. We averaged our data sets and plotted our results in Fig 4.3.1.

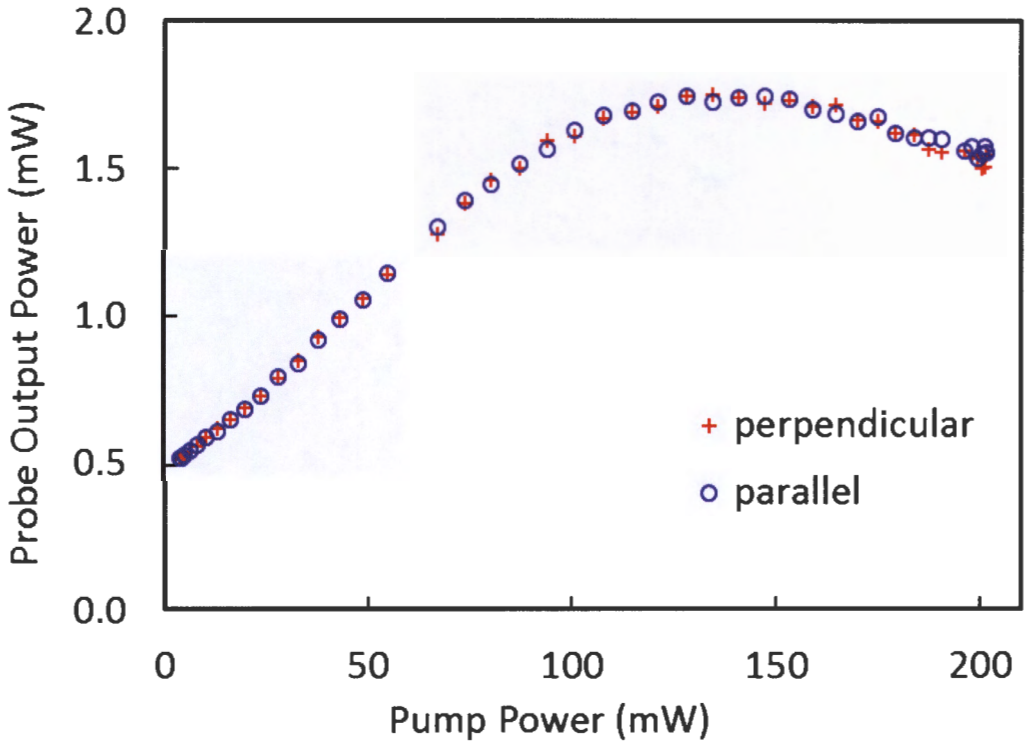

Fig 4.3.1. Output Probe Power vs Input Pump Power of gold nanorod ($d = 50$nm, $l = 145$nm) in toluene solution. Probe (1064nm) input is set to 5.0mW and is linearly polarized to either 0° or 90°. Pump (740nm) input is varied and is linearly polarized to either 0° or 90°. Data over several runs was averaged. Perpendicular and parallel signify when the linear polarization of the probe and pump were either perpendicular or parallel to each other.

For this suspension of gold nanorods in toluene, we found pump transmission to be about 73.7% (before adding long-pass filter and the pinhole) and we visually found soliton formation at a pump input power of about 192mW. From Fig 4.3.1, we see that blue circles (parallel) and red crosses (perpendicular) are almost exactly on top of each other for input pump power from 0mW to 180mW. This is as expected, since the sample should be isotropic when the soliton has yet to be formed. Between input pump power 180mW to 200mW, there starts to be a noticeable difference. To emphasize this difference, we plotted the percent difference of the perpendicular transmission with respect to the parallel transmission (Fig 4.3.2).

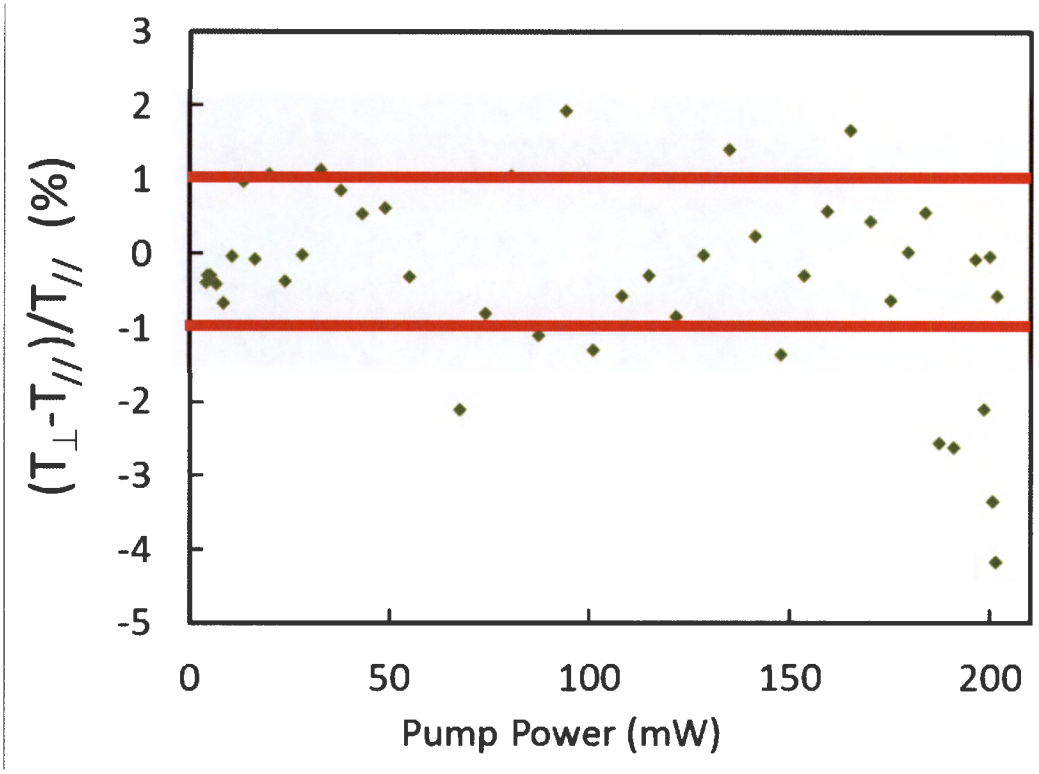

Fig 4.3.2. Percent difference of the perpendicular and parallel data from the plot in Fig 4.3.1. Considering system error from dynamic suspension, we drew two horizontal red lines at $\pm 1\%$ to show that most of the data gravitate around 0% error, until we near soliton pump power (192mW).

Noting that our soliton pumped suspension is a dynamic solution (rods moving in a fluid), we estimate there is a system error of $\pm 1\%$ due to the nature of our sample. We drew two red horizontal lines in our percent difference plot (Fig 4.3.2) at $\pm 1\%$. With the exception of a few outliers, it is clear that majority of our percent difference is at $0 \pm 1\%$.

But as we get closer to soliton pumped power (192mW) we see that we get percent difference range from -2% to -5%.

Recall that the vacuum wavenumber has the relation $k_0 = \frac{2\pi}{\lambda_0}$. Given a 1.25-cm-long sample cuvette and a 1064nm probe beam, we have $k_0 L = 7.38 \times 10^4$.

From Fig 4.3.2, we see that our greatest percent difference is -5% (lower bound). Thus,

$$\frac{T_\perp - T_{||}}{T_{||}} = \frac{T_\perp}{T_{||}} - 1 = -0.05$$

$$\frac{T_{\perp}}{T_{||}} = 0.95$$

Recall that $a = \exp\left(\left(Im(n_x) - Im(n_y)\right) k_0 L\right) = \sqrt{\frac{T(90°)}{T(0°)}}$. Taking the square root, we get

$$a = \sqrt{\frac{T_{\perp}}{T_{||}}} = \sqrt{0.95} \approx 0.9747$$

Solving for the dichroism,

$$Im(n_x - n_y) = \frac{\ln(a)}{k_0 L} = \frac{\ln(0.9747)}{7.38 \times 10^4}$$

Thus, our lower bound measured dichroism is

$$Im(n_x - n_y) = -3.46 \times 10^{-7}.$$

Repeating this for our upper bound of percent difference at -2%, we get

$$Im(n_x - n_y) = -1.37 \times 10^{-7}.$$

Comparing the Aqueous Solution with the Organic Solution

We also found that it generally required less power to create a soliton in the toluene solution than in the aqueous sample. Also, as shown in the previous chapter, the nanorods in toluene solution could be ordered with an external electric field at low frequency while the nanorods in aqueous solution could not.

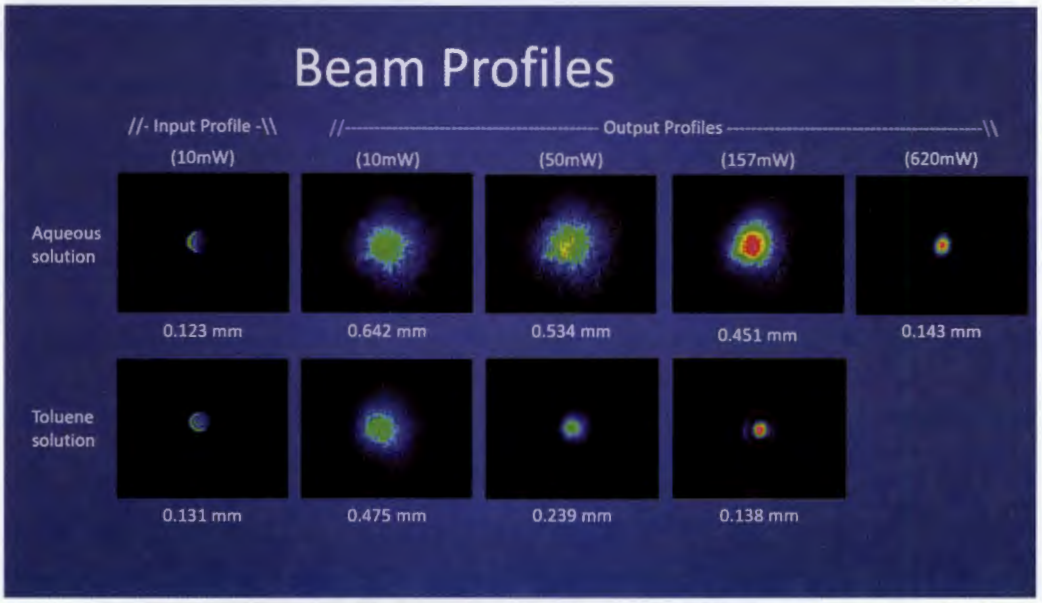

Fig 4.3.3. Beam profiles of gold nanorods ($d = 50\text{nm}$, $l = 145\text{nm}$) in aqueous and toluene solution. Optical Densities (OD) are comparable. Aqueous solution is OD1 from NanoPartz [22, 24] and toluene solution is OD5 from NanoPartz [45]. To make the toluene solution comparable to our aqueous solution we dilute our toluene solution with a sample-to-toluene ratio of 0.100mL sample + 7.000mL added toluene. Pump is at 740nm wavelength.

Fig 4.3.3 shows the beam profiles of the pump for gold nanorods in aqueous and toluene solutions. Note that the first column is a beam profile of the input beam right before it hits the front face of a 1.25-cm-long sample cuvette. The input beam sizes are comparable. The second column is the output beam right after it leave the back face of the 1.25cm sample cuvette. Again, the output beam sizes are comparable and both samples do not exhibit nonlinear effects at 10mW input pump power. The next three columns are the output beam profiles when the input pump power is at 50mW, 157mW, and 620mW. For the aqueous solution, a soliton is clearly formed when the input pump power is at 620mW. For the toluene solution, a soliton is clearly formed when the input pump power is at 157mW. We note the beam sizes for the aqueous solution at 620mW and the toluene solution at 157mW are comparable. Yet the toluene solution requires much less power.

A possible explanation for this interesting effect could be that the molecular structures of water and toluene are different. Water is a molecule that can exhibit dipole effects, affecting the Brownian motion of the rods in the sample. So an electric field from the linearly polarized pump beam can possibly also have an effect on the water molecules. On the other hand, toluene, which is a hydrocarbon, possibly does not get affected much

by our linearly polarized pump beam. As a result, the toluene solution requires less power for creating a soliton channel. Another reason could be due to the different viscosities of water and toluene.

Chapter 5: Effects of a Uniform External Field on a Soliton Pumped Nanosuspension

From chapter 3, we found that an organic solution of gold nanorods in a toluene solvent can be ordered using an applied external electric field at low frequency. This prompted us to attempt to measure dichroic properties of the pumped soliton beam created by a 740nm wavelength passing through this organic solution. In chapter 5, we then explore what effects would occur on a soliton pumped organic solution when an external electric field is applied.

5.1 Experimental Setup

We applied pump beams of various wavelengths (532nm, 740nm, 840nm, 900nm). This pump beam passes through a half-wave plate and PBS for attenuation and for the beam to be linearly polarized (p-polarized). The pump beam is then collimated with two lenses and passes through a focusing lens (focal length at 80mm).

After the focusing lens the pump beam passes through a 1.25-cm-long cuvette with sample. The sample is made of gold nanorods ($d = 50$nm, $l = 145$nm) in a toluene. The cuvette has parallel plates with a separation distance of 11.6mm.

An imaging system with neutral density filters is then setup with a CCD camera at the end to take beam profile pictures.

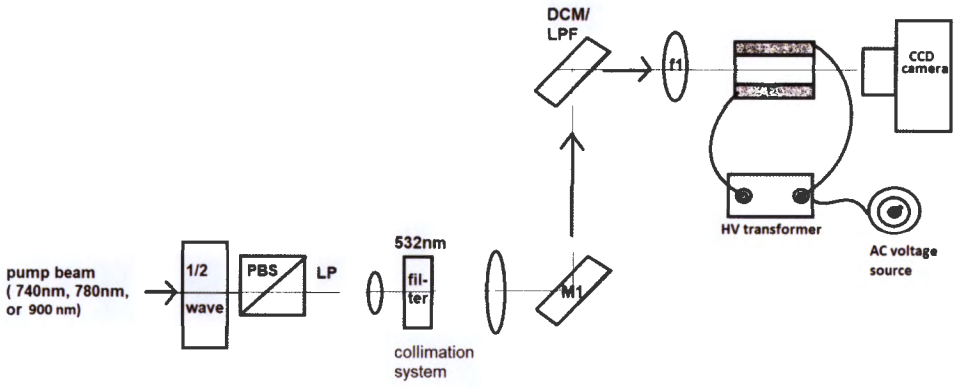

Fig 5.1.1. Schematic drawing of experimental setup to observe effects of a uniform electric field applied to a soliton pumped nanosuspension of gold nanorods (d = 50nm, l = 145nm) in toluene solvent.

5.2 Results

We first applied a p-polarized 532nm wavelength pump beam onto our organic solution. At 14mW, we were able to create a soliton. Then we applied an external uniform electric field that ranged from 0 V/mm to 538 V/mm (Fig 5.2.1). As the applied external field increases, so does the beam size (Fig 5.2.2.).

We repeated this with other wavelength (740nm, 840nm, 900nm) and got similar results. We also tried these the wavelengths when the pump beam is s-polarized (90°). Interestingly enough, it appears as though this effect is independent of wavelength, and independent of PBS orientation (which implies that it is independent of the sign of the polarizability).

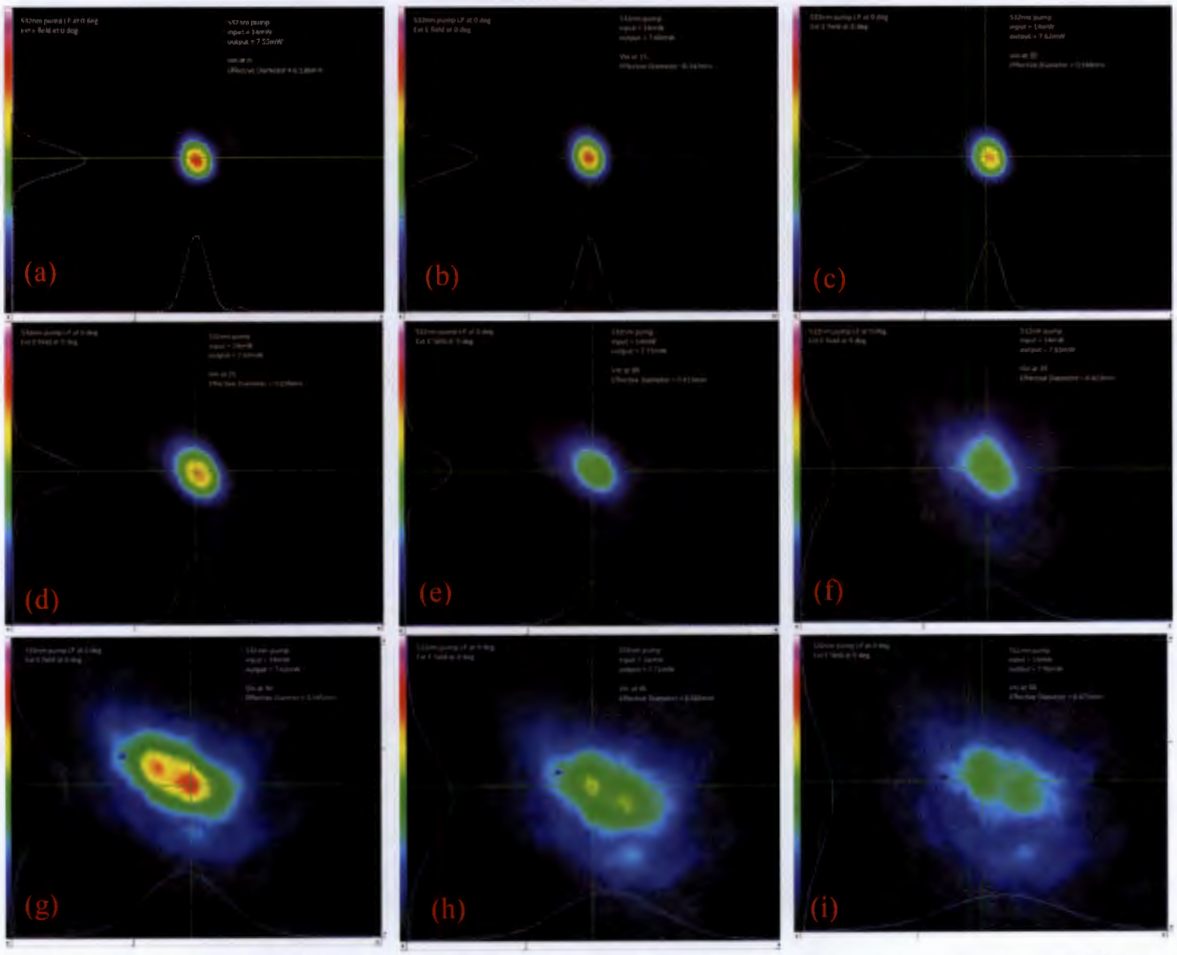

Fig 5.2.1. A toluene solution of gold nanorods (d=50nm, l=145nm) is pumped by a p-polarized 532nm wavelength laser to create a soliton at 14mW. An external electric field is then applied such that the electric field is: (a) 0 V/mm, (b) 161 V/mm, (c) 214 V/mm, (d) 269 V/mm, (e) 323 V/mm, (f) 377 V/mm, (g) 431 V/mm, (h) 484 V/mm, and (i) 538 V/mm.

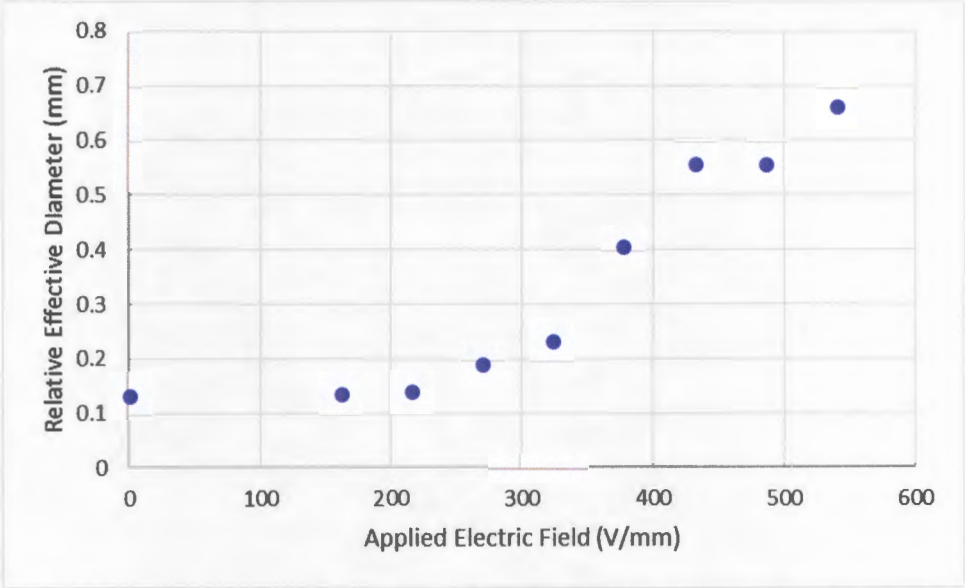

Fig 5.2.2. Plot of the relative effective diameter (mm) vs. the applied electric field (V/mm).

For various other pump wavelengths (740nm, 840nm, 900nm), we also tried applying an external electric field and got similar results. For all three cases (740nm, 840nm, 900nm), it appears that the effects are independent of PBS orientation. We got similar results when the pump polarization was perpendicular or parallel to the applied electric field.

We then applied more power to the nanosuspension until noticeable thermal effects have affected the beam shape. The first column of Fig 5.2.3. shows six cases of our nanosuspension experience thermal effects from excessive pump power. We then applied an external electric field. In all six cases, it appears that our beam shape went from a soliton broken up by thermal defocusing back to a soliton-like shaped beam.

Fig 5.2.3. Pump power in increased in a solion pump nanosuspension until noticeable thermal effects distort the beam shape. Then an external applied electric field is applied. This is down for pump wavelengths at 740nm, 840n, and 900nm for the PBS at 0° and at 90°. At 862 V/mm, it appears that a soliton-like beam shape has formed.

Currently, it should be noted that the soliton-like beam shape is not completely stable. This may be due to the low frequency oscillation of the applied electric field. Much more remains to be studied with this interesting phenomenon, such as characterizing the transmission and the change in beam size with high voltage for different wavelengths.

It appears from Fig 5.2.1. and Fig 5.2.3. that the strength of the nonlinearity of the nanorod suspension is gradually reduced as the external field is increased. The mechanism certainly merits further studies.

Chapter 6: Summary and Conclusion

In the first experiment, we attempted measuring the birefringence and dichroism in a soliton pumped nanosuspension of 145nm long rods in DI water. By probing this soliton with a linearly polarized 1064nm beam at a phase angle, $\theta_1 = -10°$, and measuring its transmission as a function of angle, θ_2, we expected to see an output transmission that is elliptically polarized. This output transmission should have a phase shift (left or right, depending on pump wavelength) and a shift up, as a result of the soliton sample's birefringent and dichroic properties due to nanorod ordering. Due to systematic error, we found reproducible results difficult to attain. Furthermore, we believe that the birefringence and dichroism to be so small that desired data may be difficult to see within the experiment's own systematic errors.

In the second experiment, by measuring transmission absorption of a linearly polarized white light spectrum going through the sample, we studied the ordering of nanorods in different solutions. Our results show that we can realize the ordering of nanorods in toluene with an AC high voltage source applied to a pair of parallel conducting plates, but we cannot observe the ordering in an aqueous solution. We infer that the dipole nature of water causes this phenomenon, which affects the Brownian motion. In the case of the aqueous solution, the voltage of the conducting plate might be driving the water molecules as much as it is the gold nanorods, disturbing the Brownian motion.

In the third experiment, we measured the dichroism of a soliton pumped nanosuspension of 145nm long rods in a toluene solution. By probing this solution with a linearly polarized 1064nm beam at different phase angles ($\theta_1 = 0°$ and $\theta_1 = 90°$) and measuring the output transmission of the sample, we were able to calculate an upper bound to the dichroic properties (-1.37×10^{-7}) of the soliton pumped nanosuspension of 145nm long rods in a toluene solution.

In the fourth experiment, we explored the effects of a uniform external electric field at low frequency on a soliton pumped in nanosuspension. Pumping by a linearly polarized beam with several wavelengths, we always observed that soliton was being destroyed and its beam size became larger as voltage on the conducting plates was applied. The output beam size at soliton power appears to get larger when we add conducting plate voltage regardless of the pump wavelength and polarization. Moreover, we observed that when the pump power was high enough to cause thermal effects, and then voltage on the conducting plates always applied, that a soliton-like shape began to form. This again was independent of the pump wavelength and polarization. Our results from our fourth

experiment appear to show that the nonlinear effects get reduced as a result of the applied external electric field. This interesting result merits further exploration and understanding.

Publications and Presentations

Alvaro, P. B.; Kelly, T. S.; Ren, Y.; Xu, H.; Chen, Z., Optically Induced Alignment of Gold Nanorods and Dichroism in Plasmonic Nanosuspension, *Frontiers in Optics 2017*, OSA Technical Digest (online) (Optical Society of America, 2017), paper LW2F.3.

Xu, H.; Kelly, T.S.; Alvaro, P.; Ren, Y.; Zhang, C.; Xiang, Y.; Chen, Z., Synthetic Optical Anisotropy via Plasmonic Resonant Tuning of Nanorod Orientation, *Conference on Lasers and Electro-Optics*, OSA Technical Digest (online) (Optical Society of America, 2018), paper FF3F.4.

Appendix

Appendix A: Ambiguity with Definition of Soliton

There was a point in our experiments that we tried to characterize the upper and lower power ranges needed to create solitons in a specific aqueous plasmonic nanosuspension (gold nanorods, length = 145nm, diameter = 50nm [24]). Unfortunately, our results were not reproducible.

Part of the reason for the lack of repeatability was the ill-defined nature of soliton. In an attempt to remedy this, we tried to take beam profile pictures at the lower range of the soliton and record its input power. We then take beam profile pictures with input pump powers slightly below and slightly above our lower limit soliton pump power.

Due to the limitations in our setup (our pump power was attenuated by a half-wave plate and polarized beam splitter), we could only attenuate input power about 70mW at a time.

But for one input pump wavelength at 830nm, we were able to capture several beam profile pictures. As seen (**Fig A.1.**), we took beam profile pictures of the output for six different input powers at the fixed wavelength of 830nm: 168mW, 251mW, 370mW, 374mW, 455mW, and 560mW.

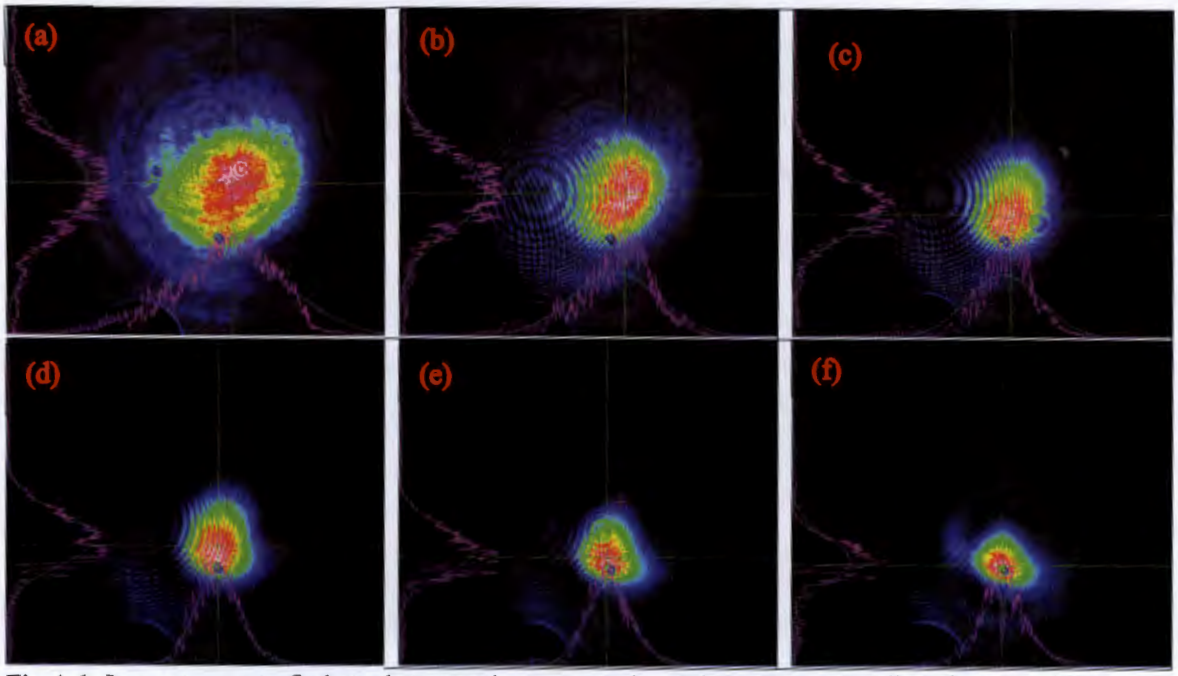

Fig A.1. In an attempt to find at what exact input power is needed to create a soliton for a specific pump wavelength 830nm and aqueous plasmonic nanosuspension (nanorods, length = 145nm, diameter = 50nm), we meticiously adjusted our input power as incrementally as possible. Limited by our setup (a halfwave plate and polarized beam splitter), we adjusted our halfwave plate every two degrees and record the input power **(a)** halfwave plate at 306 degrees, input pump power = 168mW, **(b)** halfwave plate at 304 degrees, input pump power = 251mW, **(c)** halfwave plate at 302 degrees, input pump power = 370mW, **(d)** halfwave plate at 300 degrees, input pump power = 374mW, **(e)** halfwave plate at 298 degrees, input pump power = 455mW, **(f)** halfwave plate at 296 degrees, input pump power = 560mW.

Note that we attenuated the power by changing the angle of a half-wave plate before the beam enters a polarize beam splitter. The pictures in (**Fig A.1.**) are pictures taken sequentially as the angle on the half-wave plate changes from 306 degrees to 296 degrees at a two-degree increment. This is the most accurate we can get in power attenuation.

As one can see in the six pictures, the change of the beam from low power linear diffraction to soliton is very gradual. Fig A.1.a (168mW at 306 degrees) is definitely low power linear diffraction. And Fig A.1.f (560mW at 296 degrees) is definitely a soliton. But the exact moment when soliton starts to exist still is a bit subjective. This subjectivity contributed to the inconsistency in our attempt to characterize the lower and upper input pump power limits of soliton for different pump wavelengths.

Appendix B: Importance of the Thermal Effect in Solitons

The nonlinear Schrodinger-like equation with thermal defocusing response [2] included is

$$i\frac{\partial}{\partial z}\varphi + \frac{1}{2k_0 n_b}\nabla_\perp^2\varphi + k_0(n_p - n_b)\rho V\varphi + \frac{i\sigma\rho}{2}\varphi - k_0|\Delta n_T|\varphi = 0.$$

Since the thermal effect in solitons are considered minimal, the nonlinear Schrodinger-like equation for solitons is often simplified [2] to

$$i\frac{\partial}{\partial z}\varphi + \frac{1}{2k_0 n_b}\nabla_\perp^2\varphi + k_0(n_p - n_b)\rho V\varphi + \frac{i\sigma\rho}{2}\varphi = 0.$$

Despite this, I would just like to note thermal effects do exist in solitons. One way we have noticed this is by the "sinking" feature of a soliton. As seen below (**Fig B.1.**) we take beam profile pictures of a soliton created by 730nm pump beam sent through a plasmonic nanosuspension (nanorods, length = 145nm, diameter = 50nm, in organic solvent toluene). In general, the thermal convection effect is an important phenomenon in the propagation of laser beam through liquid media [42].

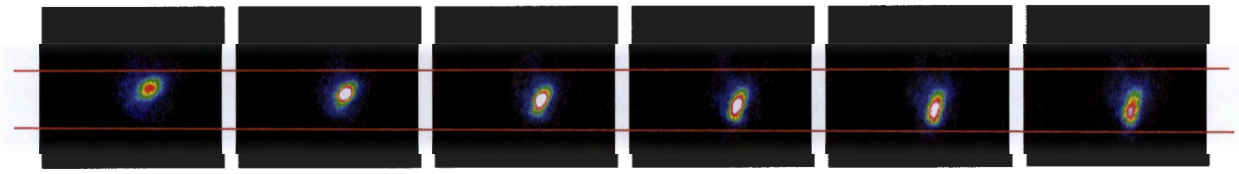

Fig B.1. Beam profiles of a soliton pumped at 730nm wavelength with 40mW input power taken over several frames. Two horizontal red lines are added to emphasize the sinking action as the soliton forms and settles into place.

Appendix C: Why certain Dichroic Mirrors do not easily maintain Polarization

During our birefringence experiment, we initially wanted to probe our soliton channel at some angle like $\theta_{probe} = 30^o$ with respect to our linearly polarized pump beam. Since this angle has a mixed polarization state relative to s and p, our linearly polarized probe beam at 30 degrees will be turned into an elliptically polarized beam after passing through the DCM.

We thought if we could find the right dichroic mirror (DMC) with transmission for both S and P polarizations relatively high and close to each other, we thought we could bypass this issue.

One example of a DCM we thought would work was the Thorlabs DMLP950 DCM [27, 28], which, for a wavelength of 1064nm, had p-polarized transmission at 99.47885895% and s-polarized transmission at 96.5320257%. Unfortunately, this DCM would still end up producing an elliptically polarized our probe beam.

We eventually, came to a discussion. In order to explain why the DCM will not preserve our linearly polarized light at an angle, we will first need to discuss Fresnel's equation and the Transfer Matrix Method.

Fresnel Equation

When a beam of light travels from one medium (with refractive index, n_1) into another medium (with refractive index, n_2), there results in a reflected beam and a refracted beam.

The Fresnel equations (named after Augustin-Jean Fresnel) describe the behavior of light when regarded as electromagnetic waves and shows what happens when traveling between media of differing refractive indices. They describe what fraction of light is reflected (and the phase shift) and what fraction of light is refracted.

We should note that there is an assumption that the interface between the media is flat and that the media are homogeneous. Also, the incident light is assumed to be a plane wave, and the effects of the edges are neglected.

Prior to Fresnel's equations, there are three laws to consider. We will employ them here without proof. The first law states that the incident, reflected, and transmitted propagation wave vectors, $\vec{k}_{i,R,T}$, are all coplanar. This plane, we call the **plane of incidence**, which also includes the normal to the surface [29, 30]. The second law, known as the **law of reflection**, states that the angle of incidence is equal to the angle of reflection [29, 30],

$$\theta_i = \theta_R.$$

Lastly, the third law, known as the law of refraction, or **Snell's law**, states that [29, 30]

$$\frac{\sin\theta_T}{\sin\theta_R} = \frac{n_1}{n_2}.$$

From these three laws, the boundary conditions arising from Maxwell's equations, and some algebra, we get Fresnel's equations for TE and TM modes [29, 30]:

for the *reflection coefficient* $r = E_R/E_i$,

$$TE\colon\ r = \frac{E_R}{E_i} = \frac{\cos\theta_i - \sqrt{n^2 - \sin^2\theta_i}}{\cos\theta_i + \sqrt{n^2 - \sin^2\theta_i}}$$

$$TM\colon\ r = \frac{E_R}{E_i} = \frac{n^2\cos\theta_i - \sqrt{n^2 - \sin^2\theta_i}}{n^2\cos\theta_i + \sqrt{n^2 - \sin^2\theta_i}}$$

and for the *transmission coefficient* $t = E_T/E_i$,

$$TE\colon\ t = \frac{E_T}{E_i} = \frac{2\cos\theta_i}{\cos\theta_i + \sqrt{n^2 - \sin^2\theta_i}}$$

$$TM\colon\ t = \frac{E_T}{E_i} = \frac{2n\cos\theta_i}{n^2\cos\theta_i + \sqrt{n^2 - \sin^2\theta_i}}$$

where n is the *relative refractive index* $n \equiv n_2/n_1$.

Fresnel's equations can be written in a different form, to describe the ratio of both reflected and transmitted E-field amplitudes to the incident E-field amplitude,

$$TE\colon\ t = r + 1$$

$$TM\colon\ nt = r + 1.$$

Recall that for Fresnel's equations we assumed that the interface is flat and the media is homogeneous. For a nonplanar surface, the reflection and transmission coefficients will also depend on scattering losses.

Transfer Matrix Method

The transfer-matrix method is a method used to analyze the propagation of light through a multilayer. This method is widely used for the design of anti-reflective coating and dielectric mirrors.

The reflection of light from a single interface between two media is described by the Fresnel equations. But, when there are multiple interfaces, like a multilayer of thin films on a substrate, the reflections themselves are also partially transmitted and then partially reflected. Depending on the exact path length, these reflections can interfere destructively or constructively.

The transfer-matrix method is based on the continuity conditions for the electric field across boundaries from one medium to another. This is governed essentially by Maxwell's equations. If the field is known at the beginning of a layer, then the field at the end of the layer can be derived from a matrix operation. This multilayer stack can then be represented as a system matrix.

The boundary condition at one interface can then be written as [46]

$$\begin{bmatrix} E_a \\ B_a \end{bmatrix} = \begin{bmatrix} \cos\delta & i\sin\delta \\ i\,\gamma_1 \sin\delta & \cos\delta \end{bmatrix} \begin{bmatrix} E_b \\ B_b \end{bmatrix},$$

Where E is the electric field, B is the magnetic field, a is the beginning boundary of the interface and b is the ending boundary of the interface. $\gamma_1 \equiv n_1\sqrt{\epsilon_0\mu_0}\cos\theta_{t1}$, where n_1 is the refractive index of the layer and θ_{t1} is the angle of refraction. δ is the phase difference that develops due to one traversal of the layer, where $\delta = k_0\Delta = \left(\frac{2\pi}{\lambda_0}\right) n_1 t\cos\theta_{t1}$ and t is the thickness of the layer.

The 2×2 matrix is called the transfer matrix of the film, represented in general by

$$\mathcal{M} = \begin{bmatrix} m_{11} & m_{12} \\ m_{21} & m_{22} \end{bmatrix}$$

For a multilayer of arbitrary number N of layers,

$$\begin{bmatrix} E_a \\ B_a \end{bmatrix} = \mathcal{M}_1 \mathcal{M}_2 \mathcal{M}_3 \ldots . \mathcal{M}_N \begin{bmatrix} E_N \\ B_N \end{bmatrix}$$

Dichroic mirrors

The Dichroic Mirrors/Beamsplitter purchased from Thorlabs [28] are composed of ion-beamed-sputtered coating films deposited on a UV fused silica substrate. Although the p-polarized and s-polarized transmission and reflection spectra of these products are very similar in the wavelength of our interest, the very nature of multilayer films makes it difficult to keep a linearly polarized beam that is not at 0° or 90° from becoming elliptically polarized at the output.

Appendix D: Matlab Scripts

In order to analyze some of our data, Matlab scripts were written to analyze and plot our data. **Transmission.m** and **absorption.m** takes white light transmission data from our Thorlabs spectrometer. While **Bidi.m** and **Bidi.m** takes laser output transmission data from our Thorlabs power meter.

Transmission.m takes transmission of the white light source through the focusing lens and the transmission of the focused white light through our nanosuspension. Then **transmission.m** plots the white light source input and the transmitted white light output so that we can compare and verify that our particular sample had a concentration with enough absorption at their two peaks ($Im(\alpha_{\perp})$ and $Im(\alpha_{||})$).

Absorption.m takes transmission of focused white light through a toluene sample only as reference, and transmission of focused white light through a gold nanorod sample with an external electric field applied at several different strengths. Then **absorption.m** plots the absorption of the sample with respect to the toluene only sample for several different strengths of applied electric field. For a cleaner look, a moving average was applied.

Bidi.m takes pump input data when the second halfwave plate is rotating and takes probe output data, when the polarization of the probe beam is at 0° and 90°. Then **Bidi.m** plots an output probe beam power vs. input pump beam power graph for two cases when the polarization of the probe beam is at 0° and 90°. Because we found a hysteresis affect in our data acquisition, we added a loop that will only include data points when the input power is increasing and ignore data point when the input power is decreasing.

BidiPerDiff.m takes the same information that **Bidi.m** takes. But instead of plotting two separate sets of data, **BidiPerDiff.m** plots the percent difference $\frac{T(0°)-T(90°)}{T(0°)+T(90°)}$. Again, we added a loop to only include data points when the input power is increasing.

transmission.m

```
clear;
white = 'white light source.txt';%the file name
sample0 = 'with sample.txt';
 whiteA=importdata(white);%import the data
Vin0=importdata(sample0);

inputA=whiteA(:,1);%wavelength
inputB=whiteA(:,2);%white
input0=Vin0(:,2);%sample

plot(inputA,inputB,'k.-','DisplayName','white');hold on;
plot(inputA,input0,'m.-','DisplayName','Vin at 0');
%cuvetteC has plate distance about 11.6mm
%Applied E is 125(Vin)/11.6 (units V*mm^-1)
Lg\d = legend('white','Vin at 0','Location','Northeast');
title(lgd,'Applied E field')
xlabel('wavelength (nm)','FontSize',15);ylabel('transmission','FontSize',15);
axis tight
set(gca,'FontSize',15);
axis([400,1000,0,1])
shg
```

absorption.m

```
clear;
white = 'Toluene only.txt';%the file name
sample0 = 'Vin at 0.txt';
sample1 = 'Vin at 20.txt';
sample2 = 'Vin at 30.txt';
sample3 = 'Vin at 40.txt';
sample4 = 'Vin at 50.txt';
sample5 = 'Vin at 60.txt';
sample6 = 'Vin at 70.txt';
sample7 = 'Vin at 80.txt';
sample8 = 'Vin at 90.txt';
sample9 = 'Vin at 100.txt';
sample10 = 'Vin at 110.txt';
sample11 = 'Vin at 120.txt';

whiteA=importdata(white);%import the data
Vin0=importdata(sample0);
Vin1=importdata(sample1);
Vin2=importdata(sample2);
Vin3=importdata(sample3);
Vin4=importdata(sample4);
```

```
Vin5=importdata(sample5);
Vin6=importdata(sample6);
Vin7=importdata(sample7);
Vin8=importdata(sample8);
Vin9=importdata(sample9);
Vin10=importdata(sample10);
Vin11=importdata(sample11);

inputA=whiteA(1:end,1);%wavelength
inputB=whiteA(1:end,2);%white

%absorptions
blah = 300;
abs0 = smoothdata(-log(Vin0(:,2)./inputB),'movmean',blah);
abs1 = smoothdata(-log(Vin1(:,2)./inputB),'movmean',blah);
abs2 = smoothdata(-log(Vin2(:,2)./inputB),'movmean',blah);
abs3 = smoothdata(-log(Vin3(:,2)./inputB),'movmean',blah);
abs4 = smoothdata(-log(Vin4(:,2)./inputB),'movmean',blah);
abs5 = smoothdata(-log(Vin5(:,2)./inputB),'movmean',blah);
abs6 = smoothdata(-log(Vin6(:,2)./inputB),'movmean',blah);
abs7 = smoothdata(-log(Vin7(:,2)./inputB),'movmean',blah);
abs8 = smoothdata(-log(Vin8(:,2)./inputB),'movmean',blah);
abs9 = smoothdata(-log(Vin9(:,2)./inputB),'movmean',blah);
```

```
abs10 = smoothdata(-log(Vin10(:,2)./inputB),'movmean',blah);
abs11 = smoothdata(-log(Vin11(:,2)./inputB),'movmean',blah);



plot(inputA,abs0,'k.','DisplayName','0 V/mm');hold on;
plot(inputA,abs1,'b:','DisplayName','215 V/mm');
plot(inputA,abs2,'b--','DisplayName','323 V/mm');
plot(inputA,abs3,'c:','DisplayName','431 V/mm');
plot(inputA,abs4,'c--','DisplayName','538 V/mm');
plot(inputA,abs5,'g','DisplayName','646 V/mm');
plot(inputA,abs6,'g:','DisplayName','754 V/mm');
plot(inputA,abs7,'g--','DisplayName','862 V/mm');
plot(inputA,abs8,'m:','DisplayName','969 V/mm');
plot(inputA,abs9,'m--','DisplayName','1.07 kV/mm');
plot(inputA,abs10,'r:','DisplayName','1.18 kV/mm');
plot(inputA,abs11,'r.','DisplayName','1.29 kV/mm');
%cuvetteB has distance about 11.6mm
%Applied E is 125(Vin)/11.6 (units V*mm^-1)
lgd = legend('show','Location','northeastoutside');
title(lgd,'Applied E field');
title({'2018 0419 (P1 at 0)';'E12-50-800-NPO-TOL-50';'(0.05mL sample + 1.0mL
Toluene)'});
xlabel('wavelength (nm)','FontSize',15);ylabel('absorption (\alphaL)','FontSize',15);
```

```
axis tight
set(gca,'FontSize',15);
axis([480,950,2,7])

shg
```

Bidi.m

```
clear;
round = '2';
input = ['inPut_00',round,'.txt'];%the file name
P0 = ['P1 at 0_00',round,'.txt'];
P90 = ['P1 at 90_00',round,'.txt'];
inputA=importdata(input);%import the data
P0A=importdata(P0);
P90A=importdata(P90);

%for loop will only take data when the input power is rising
count=0;
for jj=3:length(inputA)-1
   inputB1=inputA{jj};
   inputB2=inputA{jj+1};
   if str2num(inputB1(26:35))-str2num(inputB2(26:35))<0
      count=count +1;
      inputB=inputA{jj};
      inputC(count,1)=str2num(inputB(26:35));%take the number from the string.

      outputB=P0A{jj};
      PP0(count,1)=str2num(outputB(26:35));
```

```
        outputC=P90A{jj};
        PP90(count,1)=str2num(outputC(26:35));
    end
end


plot(inputC,PP0*1e3,'o');hold on;
plot(inputC,PP90*1e3,'ro');
title({['2018 0420 Round ',round],'740nm (PBS 0)'});
legend('probe beam at 0 polarization', 'probe beam at 90 polarization','location','NorthWest')
xlabel('input pump beam power (W)','FontSize',15);ylabel('Output probe beam power (mW)','FontSize',15);
axis tight
set(gca,'FontSize',15);
shg
```

BidiPerDiff.m

```
clear;
round = '1';
input = ['inPut_00',round,'.txt'];%the file name
P0 = ['P1 at 0_00',round,'.txt'];
P90 = ['P1 at 90_00',round,'.txt'];
inputA=importdata(input);%import the data
P0A=importdata(P0);
P90A=importdata(P90);

%for loop will take data when the input power is rising
count=0;
for jj=3:length(inputA)-1
   inputB1=inputA{jj};
   inputB2=inputA{jj+1};
   if str2num(inputB1(26:36))-str2num(inputB2(26:35))<0
      count=count +1;
      inputB=inputA{jj};
      inputC(count,1)=str2num(inputB(26:35));%take the number from the string.

      outputB=P0A{jj};
      PP0(count,1)=str2num(outputB(26:35));
```

```
        outputC=P90A{jj};
        PP90(count,1)=str2num(outputC(26:35));
    end
end


plot(inputC,((PP0*1e3)-(PP90*1e3))./((PP0*1e3)+(PP90*1e3)),'o');hold on;
title({['Percent Difference Round ',round],'740nm (PBS at 0)'});
xlabel('input pump beam power (W)','FontSize',15);ylabel('Output probe beam power (mW)','FontSize',15);
axis tight
set(gca,'FontSize',15);
shg
```

Bibliography

[1] Scott Russell, J. (**1844**). "Report on waves". *Fourteenth meeting of the British Association for Advancement of Science.*

[2] Fardad, S.; Salandrion, A.; Heinrich, M.; Zhang, P.; Chen, Z.; Christodoulides D. N. Plasmonic Resonant Solitons in Metallic Nanosuspensions *Nano Lett.* 14(5):2498—2504 (**2014**) PMID: 24697412.

[3] Salandrino, A.; Fardad, S.; Christodoulides, D. N. J. Generalized Mie Theory of Optical Forces *Opt. Soc. Am.* B 29, 855-866 (**2012**).

[4] El-Ganainy, R.; Christodoulides, D. N.; Rotschild, C.; Segev, M. Soliton dynamics and self-induced transparency in nonlinear nanosuspensions *Opt. Express*, 15(16):10207–10218, (Aug **2007**).

[5] Selhuber-Unkel, C.; Zins, I.; Schubert, O.; Sonnichsen, C.; Oddershede, L. B. Quantitative Optical Trapping of Single Gold Nanorods *Nano Lett.* 8, 2998—3003 (**2008**).

[6] Pelton, M.; Liu, M. Z.; Kim, H. Y.; Smith G.; Guyot-Sionnest, P.; Scherer, N. F. Optical Trapping and Alignment of Single Gold Nanorods by using Plasmon Resonances *Opt. Lett.* 31, 2075—2077 (**2006**).

[7] Bonin, K. D.; Kourmanov, B.; Walker, T. G. Light torque nanocontrol, nanomotors and nanorockers *Opt. Express* 10, 984—989 (**2002**).

[8] Cox A. J.; DeWeerd A. J.; Linden J. An experiment to measure Mie and Rayleigh total scattering cross section *Am. Jour. Phys.* 70, 620 (**2002**); doi 10.1119/1.1466815

[9] http://hyperphysics.phy-astr.gsu.edu/hbase/phyopt/biref.html

[10] Drazin, P. G.; Johnson, R. S. "Solitons: an introduction, Cambridge texts in applied mathematics." *Cambridge University Press* (**1989**).

[11] Ashkin, A. Acceleration and Trapping of Particles by Radiation Pressure *Phys. Rev. Lett.* 24, 156 (**1970**).

[12] Man W.; Fardad S.; Zhang Z.; Heinrich, M.; Christodoulides D. N.; Chen, Z. Optical Nonlinearities and Enhanced Light Transmission in Soft-Matter Systems with Tunable Polarizabilities *Phys. Rev. Lett.* 111, 218302 (**2013**).

[13] Smith, P.W;, Maloney, P. J.; Ashkin, A. Use of a Liquid Suspension of Dielectric Spheres as an Artificial Kerr Medium *Opt. Lett.* 7, 347 (**1982**).

[14] Gordon, J.P. Radiation Forces and Momenta in Dielectric Media *Phys. Rev.* A 8, 14 (**1973**).

[15] Terbor, R. A.; Torres, J. P.; Volke-Sepulved, K. Steering and Guiding Light with Light in a Nanosuspension *Opt. Lett.* 38, 5284-5287 (**2013**).

[16] Reyna, A. S.; de Araújo, C. B. Guiding and Confinement of Light Induced by Optical Vortex Solitons in a Cubic-Quintic Medium *Opt. Lett.* 41, 191-194 (**2016**).

[17] Kelly, T. S.; Ren, Y.; Samadi, A.; Bezrydina, A.; Christodoulides, D.; Chen, Z. Guiding and Nonlinear Coupling of Light in Plasmonic Nanosuspensions *Opt. Lett.* 41, 3817-3820 (**2016**).

[18] Ren, Y.; Kelly, T. S.; Zhang, C.; Xu, H.; Chen, Z. Soliton-mediated Orientational Ordering of Gold Nanorods and Birefringence in Plasmonic Suspensions *Opt. Lett.* 42, 627-630 (**2017**).

[19] Adams, D. J. Theory of the Dielectric Constant of Ice *Nature* 293, 447-449 (08 Oct **1981**); doi: 10.1038/293447a0

[20] Ruijgrok, P. V.; Verhart, N. R.; Zijlstra, P.; Tchebotareva, A. L.; Orrit, M. Brownian Fluctuations and Heating of an Optically Aligned Gold Nanorod *Phys. Rev. Lett.* 107, 037401 (**2011**).

[21] Bohren, C. F.; Huffman, D. R. Absorption and Scattering of Light by Small Particles *Wiley-VCH* (**2007**), pp. 130-157.

[22] https://www.nanopartz.com/bare_gold_nanorods.asp

[23] https://www.nanopartz.com/Current%20Stock%20COAs/A12-50-600-CTAB.pdf

[24] https://www.nanopartz.com/Current%20Stock%20COAs/A12-50-800-CTAB.pdf

[25] http://www.macs.hw.ac.uk/~chris/scott_russell.html

[26] https://www.learner.org/courses/chemistry/text/text.html?dis=U&num=Ym5WdElURS9OQ289&sec=Ym5WdElUQS9OQ289

[27] https://www.thorlabs.com/thorproduct.cfm?partnumber=DMLP950

[28] https://www.thorlabs.com/newgrouppage9.cfm?objectgroup_id=3313&pn=DMLP950

[29] Pedrotti, F.L.; Pedrotti, L.S. *Introduction to Optics* Prentice-Hall Inc. (**1993**) 2nd Edition, pp. 407-425

[30] Griffiths, D. J.; *Introduction to Electrodynamics* Prentice-Hall (**1999**) 3rd Edition, pp. 386-392

[31] Hansen, P. M.; Bhatia, V. K.; Oddershede, L. Expanding the Optical Trapping Range of Gold Nano Particles *Nano Lett.* 5, 10, 1937-1942 (2005)

[32] Novorny, L.; Hecht, B. Principles of Nano-Optics Cambridge University Press (2006) pp. 427-428.

[33] Zhan, Q. Trapping Metallic Rayleigh Particles with Radial Polarization *Opt. Exp.* 12, 15, 3377-3382 (2004)

[34] van der Zande, B. M. I.; Koper, G. J. M.; Lekkerkerker, H. N. W. Alignment of Rod-Shaped Gold Particles by Electric Fields *J. Phys. Chem.* B 103, 5754-5760 (1999)

[35] Fontana, J. P. Self-Assembly and Characterization of Anisotropic Metamaterials, thesis *Kent University* (2011)

[36] Fontana, J.; Naciri, J.; Rendell, R.; Ratna, B. R. Macroscopic Self-Assembly and Optical Characterization of Nanoparticle-Ligand Metamaterials *Adv. Opt. Mat.* (2013)

[37] Fontana, J.; Naciri, J.; Rendell, R.; Ratna, B. R. Macroscopic Self-Assembly and Optical Characterization of Nanoparticle-Ligand Metamaterials, Supporting Information (2013)

[38] Fonta, J.; Naciri, J.; Rendell, R.; Ratna, B. R. Macrosocpic Self-Assmembly and Optical Characterization of Nanoparticle-Ligand Metamaterials, Supporting Information, video (2013)

[39] Fontana, J.; da Costa, G. K. B; Pereira, J. M.; Naciri, J.; Ratna, B. R.; Palffy-Muhoray, P.; Carvalho, I. C. S. Electric Field Induced Orientational Order of Gold Nanorods in Dilute Organic Suspensions *Appl. Phys. Lett.* 108, 081904 (2016)

[40] https://www.thorlabs.com/drawings/2c38e51ff9edb0ee-56A0B172-FFEB-D0A0-54E49F44DD7B56A5/PBS252-AutoCADPDF.pdf

[41] Pedrotti, F.L.; Pedrotti, L.S. *Introduction to Optics* Prentice-Hall Inc. (**1993**) 2nd Edition, pp. 298-322

[42] Karimzadeh, R. Spatial Self-Phase Modulation of a Laser Beam Propagating through liquids with Self-Induced Natural Convection Flow *J. Opt.* 14 095701 (9pp) (2012).

[43] https://www.nanopartz.com/Current%20Stock%20COAs/A12-10-2100-CTAB.pdf

[44] https://www.nanopartz.com/Current%20Stock%20COAs/A12-25-1400-CTAB.pdf

[45] https://www.nanopartz.com/organic_gold_nanoparticles.asp

[46] Pedrotti, F.L.; Pedrotti, L.S. *Introduction to Optics* Prentice-Hall Inc. (**1993**) 2nd Edition, pp. 391-406

[47] Alvaro, P. B.; Kelly, T. S.; Ren, Y.; Xu, H.; Chen, Z., Optically Induced Alignment of Gold Nanorods and Dichroism in Plasmonic Nanosuspension, *Frontiers in Optics 2017*, OSA Technical Digest (online) (Optical Society of America, **2017**), paper LW2F.3.

[48] Xu, H.; Kelly, T.S.; Alvaro, P.; Ren, Y.; Zhang, C.; Xiang, Y.; Chen, Z., Synthetic Optical Anisotropy via Plasmonic Resonant Tuning of Nanorod Orientation, *Conference on Lasers and Electro-Optics*, OSA Technical Digest (online) (Optical Society of America, **2018**), paper FF3F.4.